Sensing Snow Over Arctic Sea Ice Using GNSS Interferometric Reflectometry

Sarah Zhang

ABSTRACT

GNSS Interferometric Reflectometry (GNSS-IR) is a technique that uses reflected GNSS signals, which interfere with direct signals at the GNSS receiver, to derive frequent measurements of reflector height – the distance between the receiver antenna's phase center and the horizontal reflecting surface. This study explores the potential of GNSS-IR to measure and monitor snow on Arctic sea ice using a small-scale network of 12 identical GNSS instruments deployed in March 2021 as part of the Sea Ice Dynamics Experiment (SIDEx). Despite GNSS-IR traditionally requiring stationary receivers, this study demonstrates using a stationary receiver in Colorado that dynamic receivers still yield accurate reflector height observations. GNSS-IR using the SIDEx observations provided centimeter-level precision reflector heights, which can be further refined by accounting for azimuthal variation. The analysis of the reflector heights over time reveals seasonal trends on the sea ice. Comparison with in-situ ice mass balance buoy snow depth, air temperature, and water temperature observations further support the snow changes observed in GNSS-IR reflector heights. Future research should focus on converting reflector height measurements to snow depths, expanding the network of receiver stations, and incorporating remote sensing and additional in-situ data for validation purposes. Overall, GNSS-IR is a promising technique for studying the consequences of climate change in remote regions, such as the Arctic, that provides measurements more frequently and to higher spatial resolution than remote sensing.

KEYWORDS

cryosphere, seasonal snow, sea ice dynamics, melt pond, remote sensing

INTRODUCTION

As climate change continues to worsen, increases in surface air temperatures are exacerbated in the Arctic in comparison to lower latitudes, which is known as Arctic amplification (Previdi et al. 2021). Warming associated with Arctic amplification is primarily produced by sea ice loss; therefore, sea ice is gradually becoming thinner and younger with the progression of climate change (Kumar et al. 2010). The presence of snow on sea ice is an important regulator of sea ice thickness. The high surface albedo of snow is greater than that of ice and subsequently creates a net cooling effect for the ice. However, other impacts of the snow include its thermal insulating properties and its ability to easily warm, cool, and melt in comparison to ice. Both of these properties have warming effects on the ice, though the albedo's cooling effects overshadow them (Ledley et al. 1991). Therefore, close monitoring of snow levels in the Arctic is necessary as sea ice diminishes.

Past pan-Arctic snow measurement methods are limited and leave room for improvement. For example, in-situ snow depth measurements can be taken with Magnaprobes (Sturm and Holmgren 2018), though these only provide point measurements and require extensive resources to execute in the Arctic. Furthermore, the snow depths can be modeled (Kohler et al. 2006), but these estimates cannot be completely validated as there is no extensive observational data for comparison. Remote sensing observations lack granularity, providing weekly or monthly snow cover measurements for kilometer-scale grid cells. More recently, pan-Arctic snow depths were derived using remote sensing (Kacimi and Kwok 2022), but this method has yet to be validated. As a result, there have been few recent and consistent measurements of Arctic snow depths.

The Global Navigation Satellite System-Interferometric Reflectometry (GNSS-IR) technique has previously been used to measure snow depth (Gutmann et al. 2011, Larson et al. 2009, Larson and Nievinski 2013), so I explore its application to Arctic snow in this study. GNSS-IR provides daily measurements of the receiver station's surroundings, meters away. Not only does it provide precise and frequent measurements, but GNSS-IR also does not require additional infrastructure for its implementation (Larson et al. 2016). Existing GNSS instrumentation, i.e. ground-based receiver stations and GNSS satellite constellations, already collect the necessary data to perform GNSS-IR. The technique uses signals reflected off a planar surface surrounding the receiver that interfere with direct signals at the GNSS receiver, known as multipath (Larson 2022) (Figure 1). The receiver can detect this interference as noise, which is represented by the signal-to-noise ratio (SNR). The SNR is related to the reflector height (h_R) which is the antenna's phase center height above the reflecting surface. In summary, GNSS-IR allows for the receiver's observed SNR to be used to derive frequent h_R measurements and observe changes.

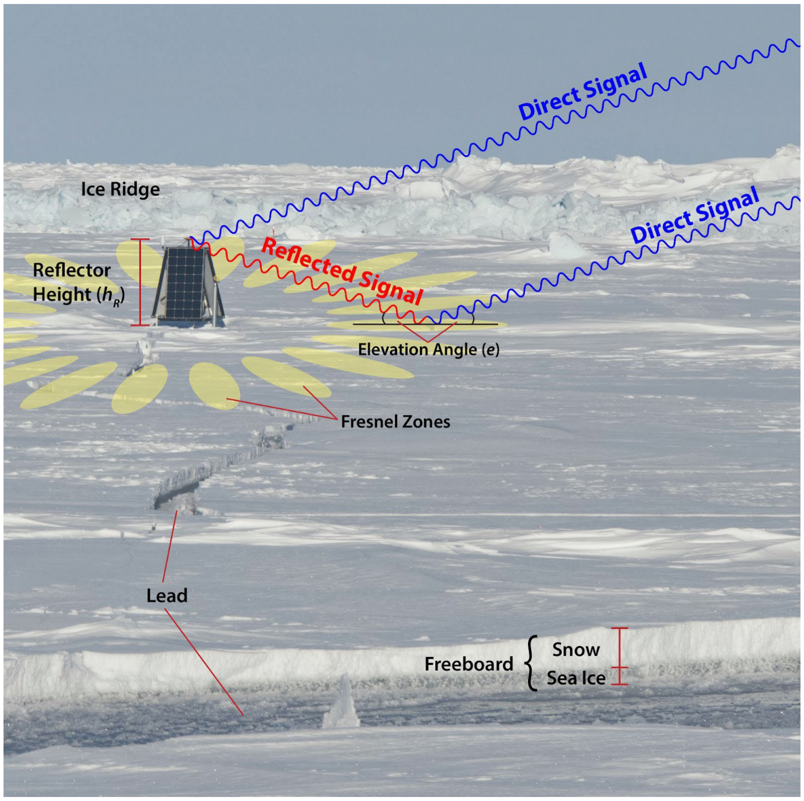

Figure 1. Visualization of the GNSS-IR process on an Arctic sea ice floe. Incoming direct signals may reflect off of the snow, at a given elevation angle, within the Fresnel zones, interfering with itself. This interference is detected at the receiver. The surrounding region of this receiver illustrates the possible variations in physical surroundings, such as ice ridges and a lead.

This study aims to address how GNSS-IR can be used to measure snow depths on Arctic sea ice. Specifically, it evaluates (1) if GNSS-IR can be effectively used in dynamic receiver station scenarios, (2) the precision of h_R measurements amongst different stations, and how they can be improved, and (3) how the GNSS-IR snow observations compare temporally, in addition to with in-situ measurements. Observations obtained from The Sea Ice Dynamic Experiment (SIDEx) will be used to explore these topics in the Arctic, providing both SNR observables for GNSS-IR and in-situ ice mass balance buoy snow depths.

METHODS

Data description

This study used data collected during the Sea Ice Dynamic Experiment (SIDEx), which consisted of a small-scale (~5 km) network of 12 autonomous GPS ice-anchored buoys in the Beaufort Sea of the Arctic Ocean (Figure 2). The buoys were deployed in March 2021 with the mission of improving understanding of sea ice mechanics and dynamics. Equipped with geodetic-quality GPS antennas, the SIDEx buoys obtain the SNR observables necessary for h_R calculations with GNSS-IR. I examined data collected in March 2021, as many of the receivers collected little-to-no data after this month due to technical issues of the receivers.

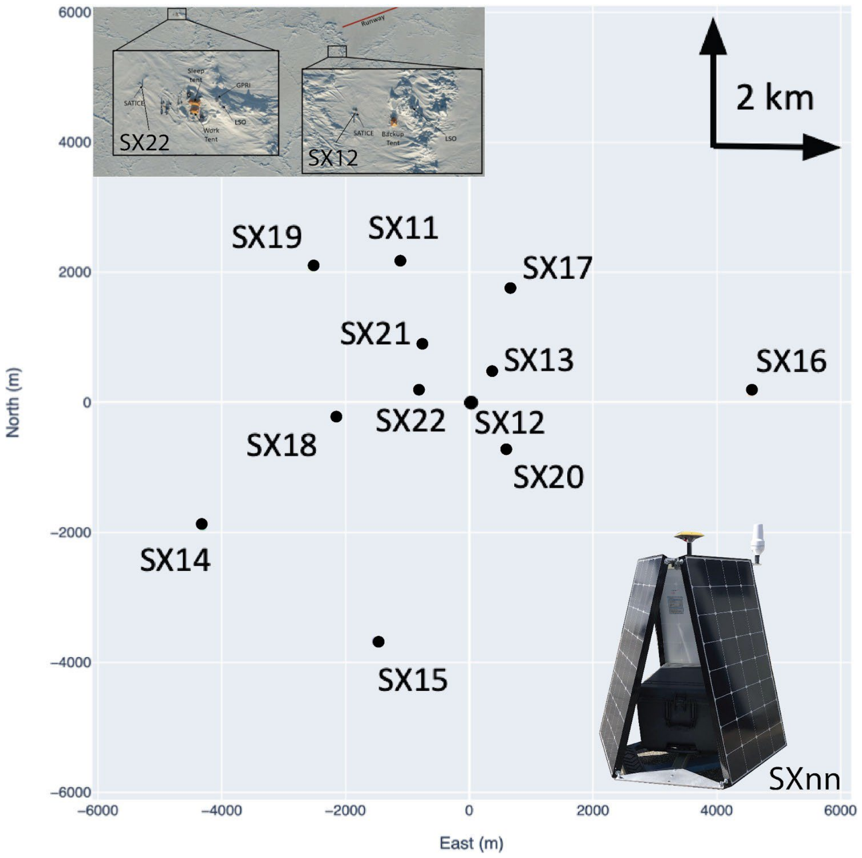

Figure 2. Location of the SIDEx stations deployed on Arctic sea ice. The stations are located in terms of distance from SX12, in meters. SX22 and SX12 (top left) were deployed in proximity to the researchers' camps and other instrumentation. An example SIDEx receiver station can be seen in the bottom right, labeled with SX and the station number, nn.

Using the SNR measured by the receiver, the h_R can be derived. The relationship between SNR and h_R can be expressed using a function of elevation angle e (Equation 1).

$$SNR(e) = Asin(\frac{4\pi h_R}{\lambda} sin(e) + \phi) \qquad (1)$$

A corresponds to the amplitude, dependent on the transmitted GNSS signal's power. λ is the wavelength of the transmitted signal, and ϕ is the phase constant (Dahl-Jensen et al. 2022). Given that SNR is observed in GNSS-IR, the equation can be simplified using the general sinusoidal function (Appendix A). As a result, the h_R term is related to the frequency of the SNR (Equation 2).

$$f_{SNR} = \frac{2h_R}{\lambda} \qquad (2)$$

From the two primary GNSS frequencies in the L-band, I used the L1 wavelength, as it provides the least noisy SNR observations. Therefore, λ can be substituted with 0.19 m, the L1 wavelength (Oxley 2017), in the formula above. The amplitude and phase constant is constant, so they are disregarded in the relationship between SNR, h_R, and elevation angle. To reduce noise in the SNR observables used for the h_R calculations, my study only employed SNR observations from elevation angles between 5° - 16°. Elevation angles larger than these bounds may include erroneous signals reflected off of the physical station, while smaller angles include reflections that are too distant from the station, so they are not as representative of the station's surroundings. Then, I applied the gnssrefl Python package (Larson 2022) to automate the process of converting the Receiver INdependent EXchange Format (RINEX) files obtained from the GPS receivers to SNR files, and then to the h_R values (Roesler and Larson 2018) (Figure 3).

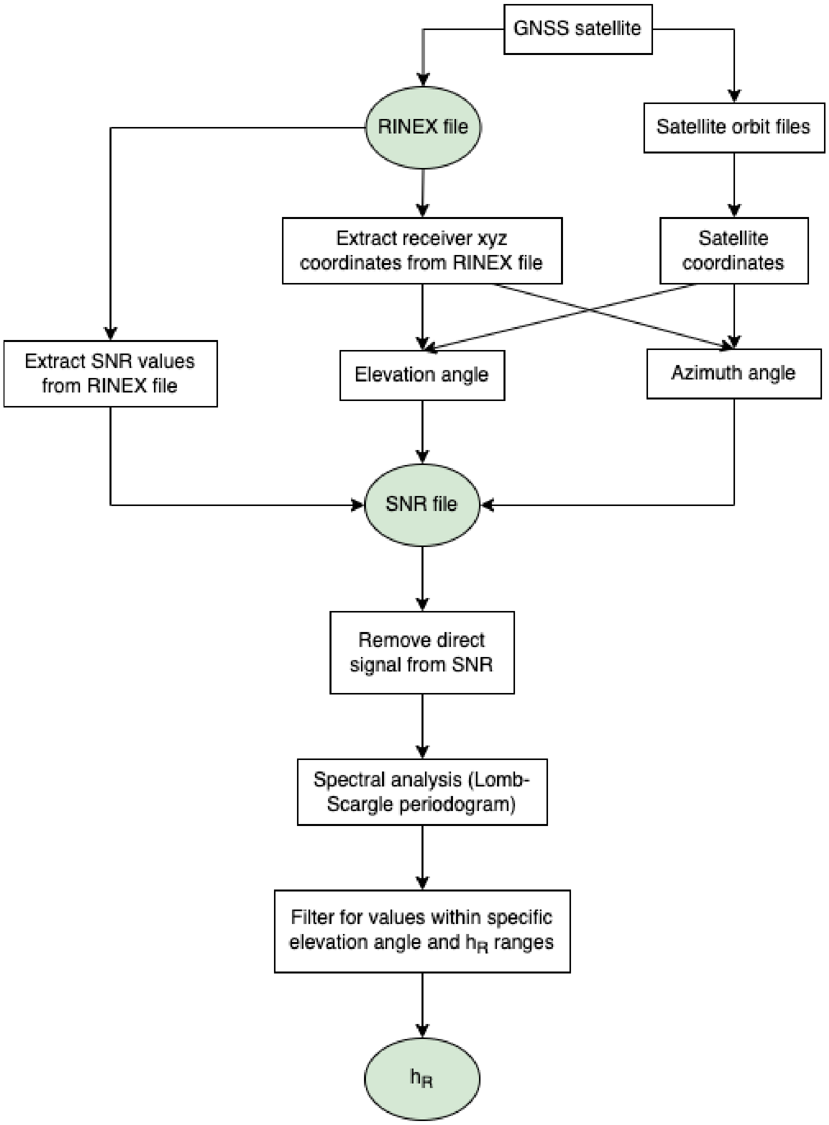

Figure 3. Flowchart illustrating the gnssrefl Python package h_R calculation method (Larson 2022). Using data contained within the RINEX file provided by the GNSS satellite, in addition to satellite orbital locations, the elevation and azimuth angles at which the SNR values were collected are determined. Then, the direct signal contribution is removed, allowing for proper spectral analysis to ultimately yield the h_R estimates.

Additionally, four autonomous ice mass balance buoys (IMBs) were deployed in the Beaufort Sea as part of the SIDEx campaign, named SX1 - SX4. Thermistor strings that stretch through the snow and ice cover into the upper ocean are equipped on each station, in addition to acoustic sensors that track the ice's top and bottom surface position. Amongst other sea ice metrics, this instrumentation provided measurements for the snow accumulation, which I used in comparison with GNSS-IR observations. Additionally, IMBs are equipped with temperature sensors, providing surface air temperature and water temperature measurements. Overall, IMBs are cost-effective alternatives to conducting field campaigns that provide a myriad of sea ice observations (Richter-Menge et al. 2006).

Empirical dynamic receiver test

Because the stations were deployed on both multi-year and first-year sea ice, the variety of Arctic conditions, including wind, temperature changes, and currents, yielded dynamic stations (Figure 4). With the station's movement, its coordinate location shifted throughout the day. As a result, the elevation angle at which a signal from a given GNSS satellite was reflected and caused multipath changed throughout the experiment. To empirically evaluate this effect, I studied the P041 station, located in Colorado. The P041 station was chosen because it has previously been used for GNSS-IR snow measurements (Larson and Nievinski 2013), its receiver antenna is stationary, and the site is planar and relatively free of obstructions. Therefore, it provided a ground-truth insight into whether errors in the station coordinates affected the h_R. This empirical study used the P041 station's data for May 11th, 2020, where there was no snowpack affecting the h_R. The SIDEx stations traveled up to 35 km per day in March 2021 (Figure 4), so I tested a 100 km station coordinate error using the P041 station as a worst-case scenario.

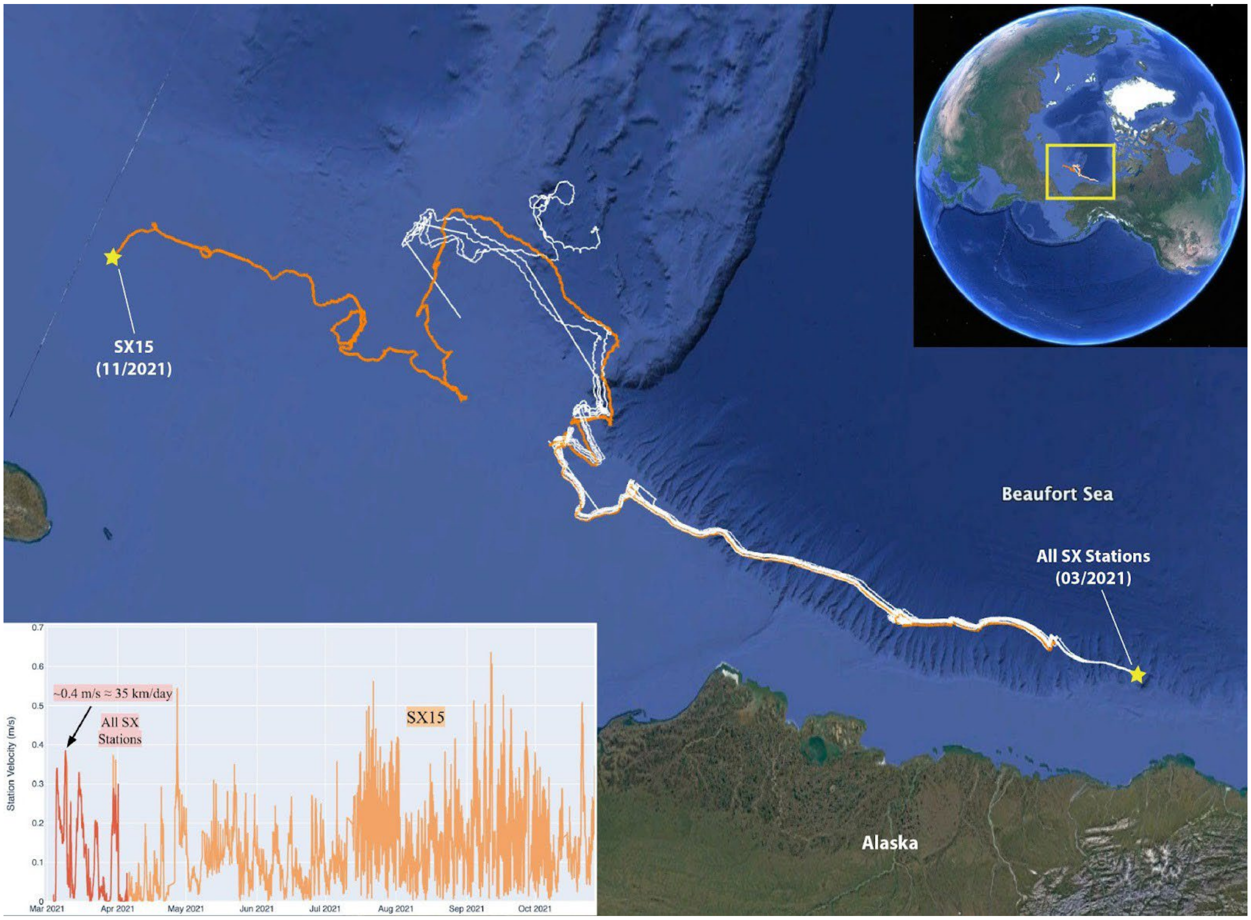

Figure 4. SIDEx station paths and velocities throughout the experiment. In the bottom left, all the stations' velocities are represented in red for March 2021. For the station velocity and station paths, SX15 is highlighted in orange. The other 11 station paths are represented in white.

Spatial variation

To explore any h_R variations and trends amongst the small-scale network of SIDEx receiver stations, each station's March 2021 h_R time series were visualized. The h_R in the time series were colored based on the azimuth, relative to the receiver station, at which the incoming GNSS signals were received. 0° corresponds to the north of the receiver, and 180° corresponds to the south of the receiver. Additionally, their means and standard deviations were determined for inter-station comparison. Using these summary statistics, I developed a model to improve the precision of the h_R estimates.

Since the physical surroundings of the stations vary by azimuth (ex. Figure 1), I devised a method to retrieve the h_R without the effect of azimuthal differences. This yielded an azimuthal model, specific to each station for a given season, which I used to detrend the March 2021 SIDEx time series data. To craft this model, each station's monthly h_R values were placed into 10° azimuth bins. Then, the mean of each bin was subtracted from each corresponding h_R in the bin, yielding the detrended data. To compare the original and detrended time series data in the same range, the monthly h_R mean was subtracted from the original h_R values for a station, preserving the original variation. I compared these results through their standard deviations and time series analysis, which gave spatiotemporal insights throughout the experiment.

Temporal comparisons

To explore any temporal variations of the snow on the sea ice, a time series of SX15 h_R is crafted. This station was able to successfully provide h_R measurements from March 1, 2021 to November 1, 2021; measurements after this period were sparse and erroneous, and therefore omitted. The h_R is subtracted from the true receiver station height, 1.3 m, yielding an estimate for the distance between the horizontal reflecting surface, typically snow, and the sea ice to which the receiver station is anchored. This is referred to as the sea ice surface anomaly. In a perfect scenario where smooth and uniform snow, with no melt ponds, is the reflecting surface and the sea ice underneath is also flat, this estimated distance represents the snow depth.

As an in-situ comparison to the GNSS-IR-derived h_R, IMB snow depths are analyzed, in addition to other ice conditions. The SX3 IMB obtained the most data, overlapping with SX15's data collection period; therefore, SX3 and SX15 snow depths are compared by being overlaid in a time series. Likewise, the SX3 air and water temperatures were explored with the SX3 snow depths to identify any possible relationships between the environmental conditions and the snow events.

RESULTS

GNSS-IR with dynamic receivers

Using errored coordinates in the P041 h_R derivation did not affect the Lomb-Scargle Periodogram (LSP), and as a result, the h_R was also unaffected (Figure 5). A 100 km change in station coordinates did not have a great effect on the h_R: any differences were within the millimeter level. Although the offset station yielded noisier SNR (Figure 5b), the LSP of both the true and offset coordinate scenarios are equivalent, yielding similar h_R.

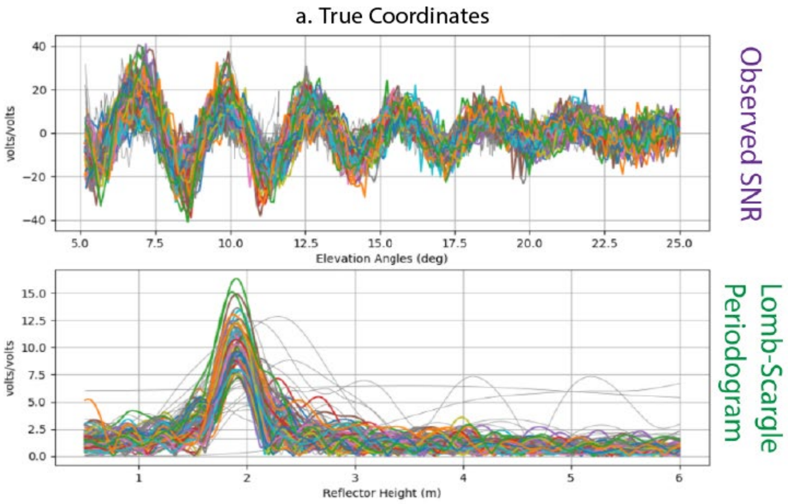
a. True Coordinates

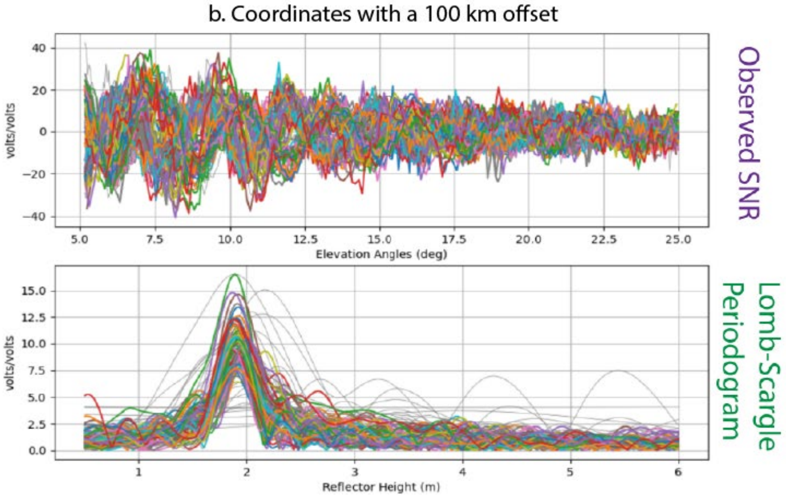
b. Coordinates with a 100 km offset

Figure 5. SNR and LSP visualizations of true and offset P041 coordinates. (a) True observed SNR and LSP from the P041 station, without any alterations. (b) Altered SNR and LSP from the P041 station, after a 100 km offset in the station coordinates. Each color represents observations from an individual satellite. The gray corresponds to failed reflections, i.e. the h_R retrieval was unsuccessful (Larson 2022). The peak location in the Lomb-Scargle Periodogram corresponds to the h_R estimate from a given satellite.

Reflector height precision and variability

Although varied amongst the 12 SIDEx stations, the March 2021 mean h_R were collected to a centimeter-level precision (Figure 6). All the stations, except for SX12 and SX20, had a mean h_R between 1.000 m and 1.500 m and a standard deviation within 0.200 m (Table 1). SX11, SX15, and SX17 had the highest precision, with standard deviations of 0.068 m, 0.067 m, and 0.054 m, respectively (Table 1). In the SX17 time series, there are many outliers, specifically from the northern direction of the station. Despite the outliers, the SX17 h_R observations have a high precision (Figure 7a).

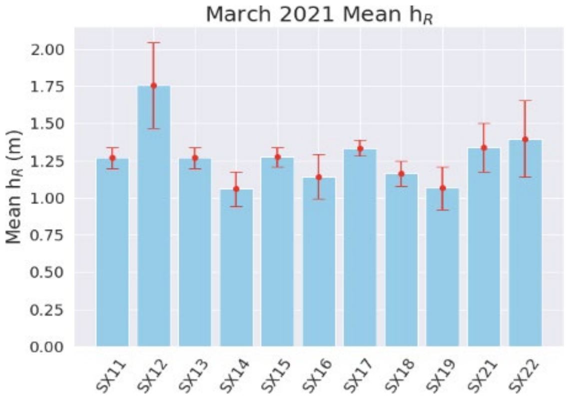

Figure 6. Summary of SIDEx March 2021 h_R. Each bar represents a station's monthly mean h_R, with error bars representing its monthly standard deviation. SX20 was omitted due to its high and variable h_R values.

Table 1. SIDEx March 2021 h_R summary statistics.

Station	Mean (m)	Standard Deviation (m)
SX11	1.268	0.068
SX12	1.757	0.289
SX13	1.267	0.071
SX14	1.058	0.115
SX15	1.273	0.067
SX16	1.143	0.148
SX17	1.335	0.054
SX18	1.162	0.084
SX19	1.064	0.143
SX20	5.011	0.962
SX21	1.339	0.164
SX22	1.397	0.258

Figure 7. Example March 2021 *h_R* time series. (a) SX17 time series, with a small standard deviation and consistent h_R measurements, despite having outliers at high azimuths (red data points). (b) SX13 time series, with a shift in the h_R on March 10. All stations' March 2021 h_R time series can be found in Appendix B.

On the other hand, there are also stations with more varied means and standard deviations. For example, SX20 has a mean h_R of 5.011 m and a standard deviation of 0.962 m, which are both very high in comparison to the other stations. Also, SX12 and SX22 had comparatively higher standard deviations, 0.289 m and 0.258 m, respectively, and SX12 also had a mean h_R of 1.757 m, slightly higher than the other stations (Table 1). Furthermore, events occurring on the sea ice can be observed through the monthly time series. A systematic increase in the h_R occurred on March 10 at both SX12 and SX13 (Appendix B and Figure 7b, respectively).

Moreover, the effect of varying physical surrounding conditions of each of the stations can be corrected by using the azimuthal model, drastically reducing the standard deviation. For instance, the variation of SX11 was reduced by 57% to 0.029 m following the application of the model (Table 2). Likewise, the original time series of SX19 observations featured a bimodal azimuthal distribution, with two distinct groupings of h_R values (Figure 8a). However, after detrending using the azimuthal model, the effect of these differences in physical surroundings (Figure 8b) is reduced. The time series is uniform following the detrending, and the SD was reduced from 0.143 m to 0.056 m (Table 2).

Table 2. Standard deviations (SD) of the SIDEx h_R before and after detrending with the azimuthal model.

Station	Original SD (m)	Detrended SD (m)	SD % Change
SX11	0.068	0.029	-57.323
SX12	0.289	0.177	-38.571
SX13	0.071	0.050	-28.842
SX14	0.115	0.054	-52.773
SX15	0.067	0.026	-60.559
SX16	0.148	0.050	-66.197
SX17	0.054	0.037	-32.166
SX18	0.084	0.065	-22.866
SX19	0.143	0.056	-60.882
SX20	0.962	0.595	-38.124
SX21	0.164	0.134	-18.682
SX22	0.258	0.160	-37.900

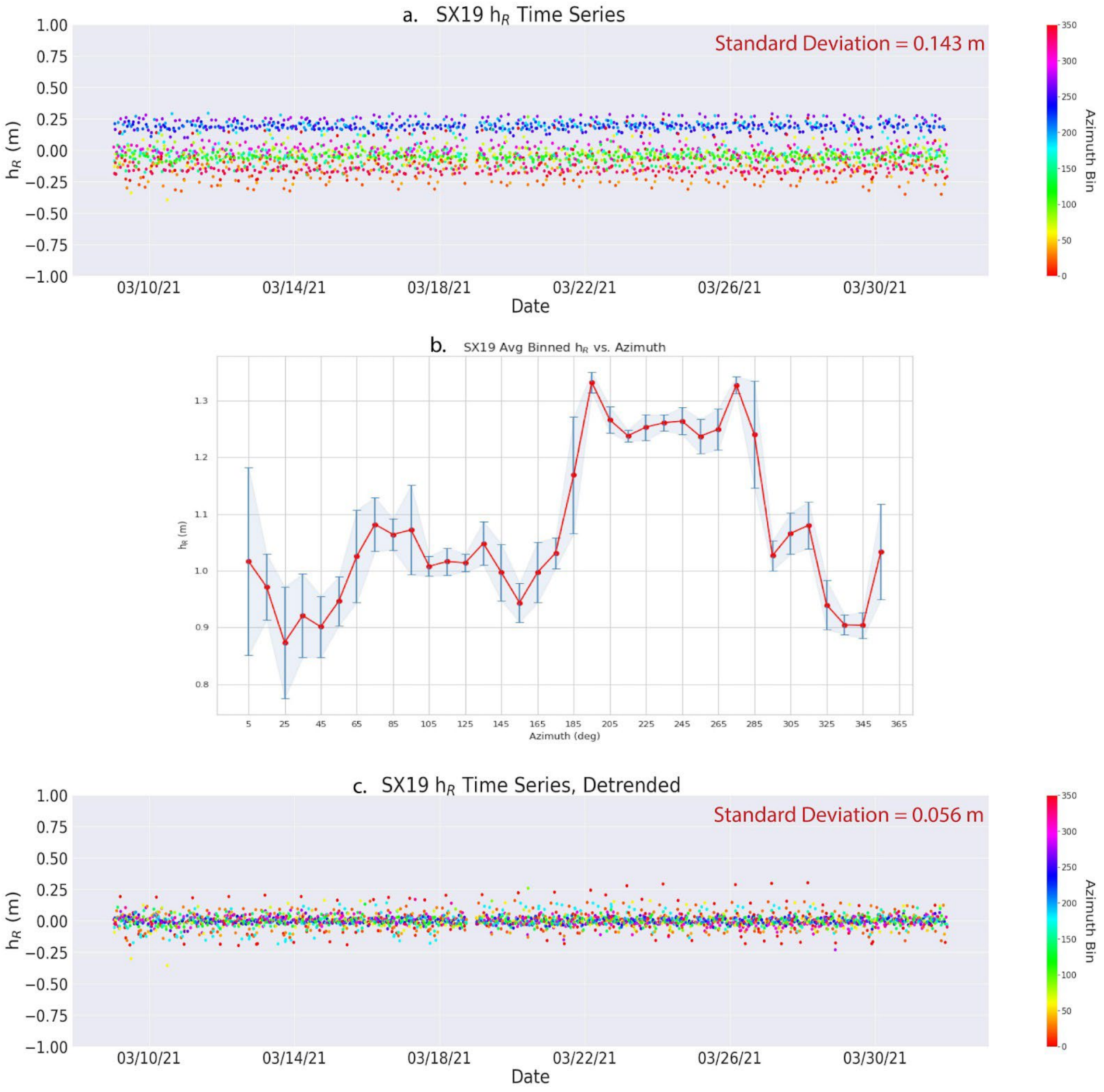

Figure 8. SX19 time series, before (a) and after (c) detrending, with each dataset's mean subtracted. The bimodal data in (a) reflects the azimuthal trends seen in (b), where the standard deviation of each mean is represented by the blue error bars. These are no longer present after detrending (c). All stations' average binned h_R vs. azimuth figures can be found in Appendix C, and their detrended time series can be found in Appendix D.

Even for irregular cases within the time series, the azimuthal model greatly reduced variation. As seen with SX13, the SD was reduced by almost 29% (Table 2), yet the systematic increase observed on March 10 is still present (Figure 9). Even for stations with noisier data, such as SX20, the h_R standard deviation was reduced following the application of the azimuthal model. The SX20 standard deviation was reduced by more than 60% (Table 2).

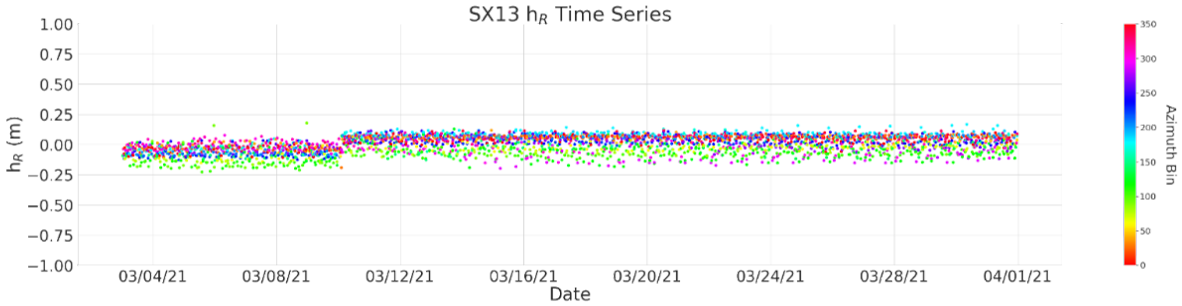

Figure 9. SX13 time series after detrending with the azimuthal model. On March 10, all of the h_R at the station increased, and this is still evident after the application of the azimuthal model.

Spatiotemporal variability and validation

Using the SX15 observations, temporal trends can be identified (Figure 10). Specifically, an increase in the h_R is seen in the late spring, i.e. May to June. Furthermore, there is very high variability in the summer months, i.e. June to September. Lastly, there is a shift in azimuth angles for which the h_R is distributed before and after the summer. In the spring, high h_R were recorded at approximately 270° azimuth, while these azimuths yielded amongst the lowest values in the fall (Figure 10).

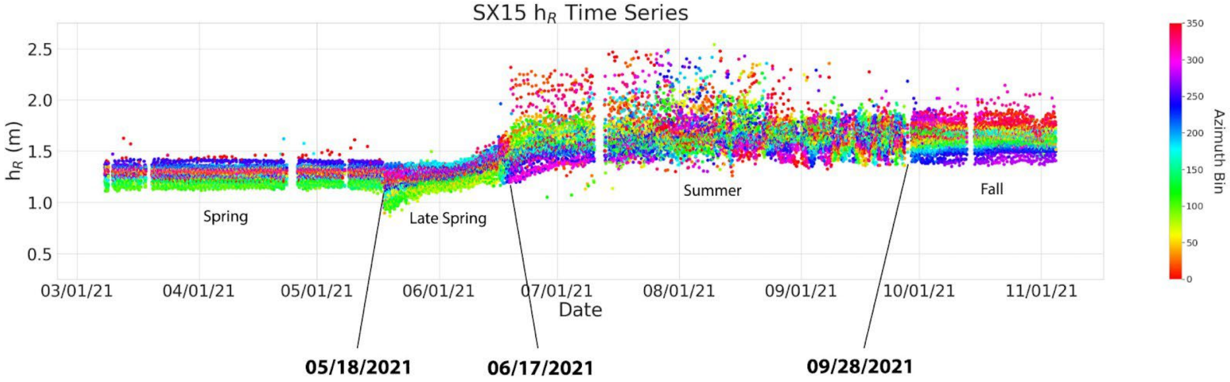

Figure 10. SX15 March to November 2021 h_R time series. Dates, where notable changes occurred in the h_R, are labeled, with the corresponding seasons labeled between them.

Before applying a vertical shift to the SX3 snow depth, the overall trends found in the SX15 h_R aligned with that of SX3 (Figure 11a). Including a vertical shift down of 0.26 m, the SX3 snow depths and the SX15 sea ice surface anomaly correspond closely in their values and trends. For example, both exhibit a sudden increase in h_R in mid-May. Additionally, they begin to decrease in mid-June and then begin to increase at the same time in September (Figure 11b).

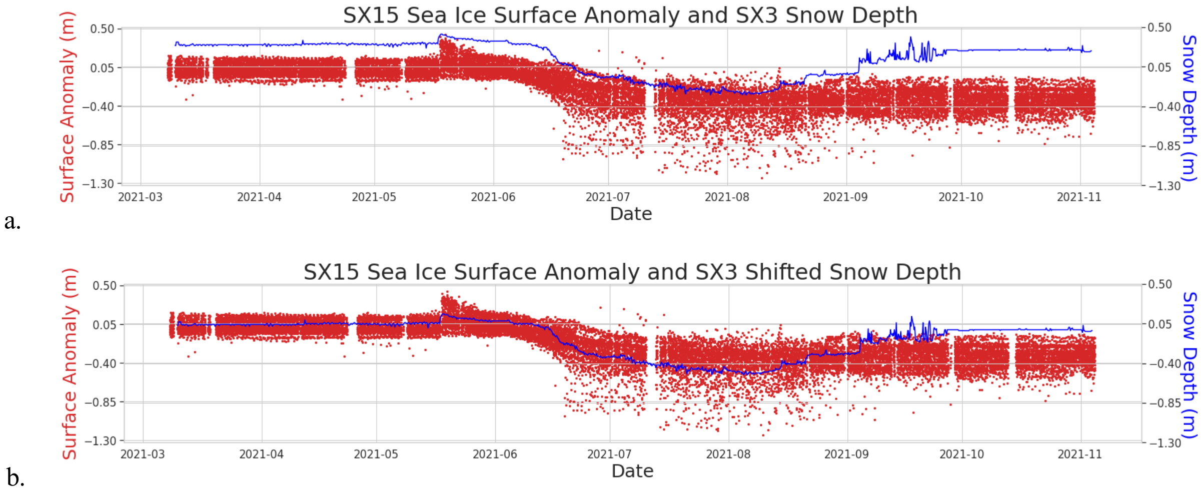

Figure 11. SX15 GNSS-IR sea ice surface anomaly and SX3 IMB snow depth. SX15 observations are represented in red, and SX3 observations are represented in blue. (a) SX15 sea ice surface anomaly and original SX3 snow depths. (b) SX15 sea ice surface anomaly and SX3 snow depths with a 0.26 m vertical shift downwards.

Comparisons between the SX3 snow depths with the air and water temperatures demonstrate potential reasons for the snow depth changes (Figure 12). When the snow depth begins decreasing in mid-May, the surface air temperature and water temperatures are increased. On the contrary, when the snow depth begins to increase in September, the air and water temperatures have cooled. Throughout the summer months, the air and water temperatures are relatively constant, sustaining the reduction in the snow depth, and possibly sea ice, over the summer. The water temperatures in the later months of the year, October to December, were overall higher than at the beginning of the year and experiment (Figure 12b). The temperature trends correspond closely to that of the SX15 snow depth, providing a background for the phenomena observed, which will be discussed in the next section.

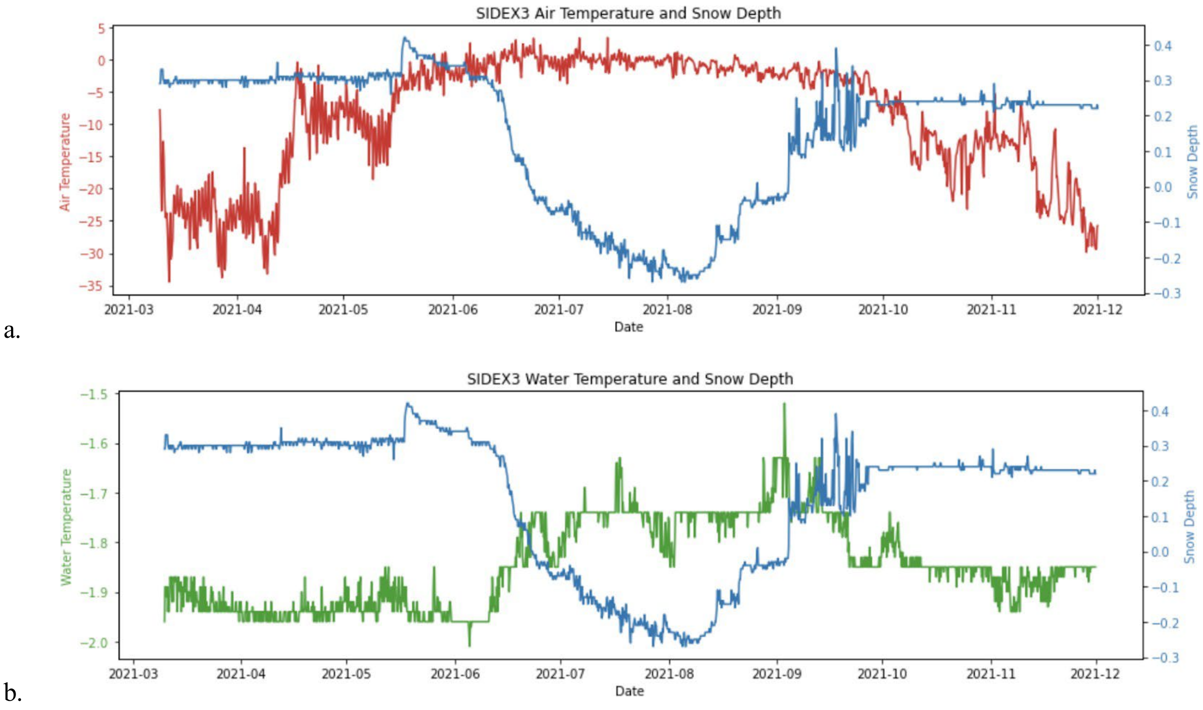

Figure 12. SX3 March to December 2021 snow depth observations in comparison to environmental conditions. (a) Air temperature (red) and snow depth (blue) comparisons from the SX3 IMB. (b) Water temperature (green) and snow depth (blue) comparisons from the SX3 IMB.

DISCUSSION

Despite only being studied in scenarios where the GNSS receiver stations are stationary, this study verifies that GNSS-IR measurements obtained from the dynamic SIDEx receiver stations are accurate. Using these observations, which offer precision on the centimeter level, differences in the stations' physical surroundings can be observed and corrected. Furthermore, the time series data illustrates the seasonal trends on the sea ice, reflecting snow depth and temperature changes observed in the in-situ data.

GNSS-IR with dynamic receivers

Errors in the station coordinates, even over vast distances, do not affect the accuracy of the h_R derivation because of the GNSS satellite arc lengths and observed nature of the SNR. SNR data is recorded during the GNSS satellite rising and setting arcs, which span about one hour in the SIDEx. As a result, the sea ice movement in this duration is not significant enough to observe notable changes in the station coordinates. Additionally, any daily change in station coordinates is negligible in comparison to the distance between the stations and GNSS satellites, which is about 20,000 km (NASA Crustal Dynamics Data Information System 2020).

As the sea ice to which a station is anchored moves, the error in its coordinates corresponds to an error in the calculated elevation angle. While the SNR depends on the elevation angle (Equation 1), this study uses observed SNR, obtained directly from the receiver, to calculate the h_R. Therefore, any change in the computed elevation angle due to an error in the coordinates will not propagate to the already-observed SNR. The error in elevation angle results in a phase change in the LSP of the detrended SNR, but phase information does not affect the LSP. The noisiness in the 100 km-offset SNR (Figure 5b) is attributed to this change in the computed elevation angle. Nonetheless, the periodicity of the SNR functions, which is used to calculate the h_R in the LSP, is preserved, as seen in the almost-identical LSP of the original and offset observations (Figure 5).

Although the GNSS-IR technique traditionally calls for a stationary receiver (Nievinski and Larson 2014), this study demonstrates that the dynamic ground-based receivers also yield accurate h_R observations; they are not affected by the coordinate changes due to sea ice movement. However, this finding is limited to the scope of a 100 km change in station coordinates, as in this study where the sea ice is moving up to 35 km per day. It is highly unlikely that a station will move more than this amount in the span of a GNSS satellite arc, so this limitation is slight. Also, techniques to account for major receiver movement can be applied; for instance, coordinates can be modeled for spaceborne GNSS-IR, where the receivers are satellites in orbit (Southwell 2020).

Reflector height precision and variability

Reflector heights are obtained using GNSS-IR, offering a centimeter-level precision, which can be further improved by accounting for azimuthal variation. The variety of standard deviations amongst the different station h_R measurements can be attributed to their respective surrounding physical environments. Although the stations form a ~5 km network, within this area, there are variations in the environment that can be observed in their h_R observations (Figure 13). The smaller SX17 h_R outliers (Figure 7) were all collected from the northern direction of the station, which means that the horizontal reflecting surface may be more elevated in this direction. A cause of the elevated reflecting surface may be greater snow accumulation or an ice ridge in this direction, but further examination with remote sensing observations can confirm this. Additionally, the station deployed on an ice ridge (Figure 13a) can be identified as SX20, with h_R values varying between 4.000 to 6.000 m (Table 1, Appendix B10). The other stations had h_R values centered below 2.000 m. This identifies SX20 as the outlier amongst the stations, with its large and variable h_R attributed to reflections from different locations on the ice ridge. Also, the noisy SX12 and SX22 h_R observations are due to their proximity to the research team's camps and instrumentation (Figure 13b). The structures interfered with the path of the GNSS signals, so not all of the h_R observations were derived from signals that reflected off the surface of the snow.

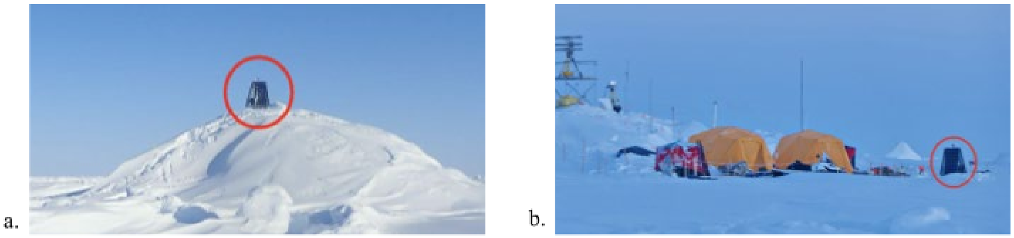

Figure 13. SIDEx receiver stations deployed at irregular locations. The station on the ice ridge can be identified as SX20 as the station's large and varying h_R corresponds to that of the image. SX12 and SX22 were deployed near the researchers' camps and instrumentation, also yielding noisier data. (Source: SIDEx Project)

Ice dynamics events can be observed in the time series. The sudden systematic increase in h_R on March 10 for SX12 (Appendix B2) and SX13 (Figure 7a) indicates a change in the entire reflector system. The increased h_R corresponds to a lowered horizontal reflecting surface. This can be attributed to snow melt or the formation of a lead, but further information is required to determine the true cause of this systematic change.

For each station, the h_R standard deviation was reduced by applying the azimuthal model (Table 2), without compromising any trends in the data. As seen with SX13, the standard deviation was greatly reduced, yet the systematic increase in h_R observed on March 10 is still present (Figure 9). This is because the azimuthal model normalizes for variation in the physical surroundings, but the systematic increase uniformly affected all of the h_R. Even for stations with noisier data, i.e. SX20, the azimuthal model also reduced the h_R standard deviation. Although the model did not fully remove the noise of this station's h_R measurements, the leftover noise in the SX20 h_R can be attributed to its deployment on an ice ridge (Figure 13a).

As further support for the efficacy of the model removing variation due to physical azimuthal differences, the bimodal distribution of the original SX19 h_R calculations (Figure 8a) no longer existed after the detrending (Figure 8b). Seen in the average h_R of each azimuthal bin (Figure 8b), SX19's physical surroundings were not uniform, with a notably higher region of h_R at about 185° - 285° azimuth. If SX19 was located near a lead, the GNSS signals would reflect from the water, which would correspond to higher h_R values at certain azimuths. Further investigation of the station is needed to establish the exact cause, but there is a clear grouping within the SX19 h_R distributions that are eliminated after accounting for physical surrounding differences.

Overall, the fine precision offered by the GNSS-IR method is better than that of remote sensing, which often offers much less precision (Tedesco et al. 2015). This study uses spectral analysis to determine the h_R from GNSS-IR, but the inverse method would provide better precision because spectral analysis is more sensitive to noise and outliers (Purnell et al. 2020). Furthermore, other techniques, such as Lidar measurements, may offer greater precision, but they are sparse in both time and space (Tedesco et al. 2015). GNSS-IR provides frequent measurements throughout the day while remotely-sensed snow depths are often collected once per month. Also, the GNSS-IR h_R measurements are for a single point, close to the receiver station, while remote sensing measurements estimate entire grid cells that typically span at least 5 km but are up to 25 km (Kacimi and Kwok 2022). This allows GNSS-IR to provide precise, point measurements, though it lacks the robustness of remote sensing observations.

Spatiotemporal variability and validation

Through the SX15 time series (Figure 10), seasonality is observed, which correlates to events also observed in situ. For instance, the increase in SX15 h_R observed in the late spring suggests snow melt and/or melt pond formation. In the Arctic, snow melt occurring in the late spring results in the formation of melt ponds (Perovich et al. 2017). Also in the Beaufort Sea, Hwang et al. 2017 observed snow melt, connecting to warming air temperatures, in mid-June, which is similar to the phenomena observed at SX15. They observed that the surface melt then led to the melt pond formation, and subsequently pond drainage, ultimately leading to breakage and the summer ice floes. The SX15 high summer variability suggests that the GNSS signals are no longer reflecting off of the surface of the snow. Instead, they may be reflecting off of melt ponds and/or the surface of the ocean, after ice breakage. As the melt continues and accelerates, the melt ponds grow, both in area and depth. As a result, the area of snow and sea ice surface diminishes, and deeper melt ponds melt through the ice, to the ocean. Once a pond melts through to the ocean, the melting rate increases (Perovich et al. 2003). Finally, in the fall, the SX15 h_R observations are less variable than in the summer, indicating the beginning of freeze-up. Perovich et al. 2009 observed melt ponds freezing and lead formation on Arctic sea ice beginning in September, in addition to new snow accumulation, which parallels the SX15 findings.

Lastly, the change in the SX15 h_R azimuth angle suggests physical rotation by the station during the summer months. While the highest h_R values were observed from about 225° azimuth in the spring, this azimuth angle yielded the lowest h_R measurements in the fall, with the highest being observed from about 325°. The shift in azimuths and their corresponding h_R measurements match with a station rotation of about 100°.

When compared with the SX15 h_R time series, the SX3 snow depth trends correspond to the h_R trends (Figure 11). The vertical shift to match the SX3 snow depths to the SX15 sea ice surface anomalies may be attributed to calibration differences of the instrumentation on the sea ice. The stations' simultaneous changes, i.e. increase in snow depth and decrease in h_R, and vice versa, demonstrate that the changes in h_R can be attributed to snow melt and accumulation. When the snow melts, the distance between the horizontal reflecting surface, which is the air-snow interface (or air-water, air-ice interface if all of the snow is melted), increases. In the summer, the snow depth is at a minimum, and the variation in the h_R is high, which provides further evidence that the GNSS reflections occurred off of melt ponds on the surface of the sea ice. Lastly, the h_R variation is reduced and constant when the snow begins to accumulate in September 2021.

Likewise, the water and air temperature measured by SX3 also support the changes observed in the snow depths, and ultimately SX15 h_R. When the snow depth begins to decrease in June, both the water and air temperatures increase with similar timings (Figure 12). This correspondence between the snow depth, water temperature, and air temperature is seen again in September 2021, when the temperatures fall and snow reaccumulates (Figure 12).

This study is limited by the lack of in-situ measurements and images at each GNSS-IR receiver station. With this information, the events and changes that occurred throughout the time series could be precisely validated. The IMB observations provide an approximate comparison for confirming events that occurred at SX15, but SX3 is over 10 km away from SX15. Additionally, this study does not include winter observations, i.e. December to February, and the summer observations feature very high variability. Therefore, the strength of the observations is limited to the seasons in which GNSS signal reflections are stable, i.e. spring and fall, so further studies are required in the region for a comprehensive review of the snow seasonality.

Future directions

Using the existing GNSS-IR h_R observations, further analysis can be done. First, all h_R measurements should be converted to snow depths, by subtracting the receiver station height and also accounting for whether the signal penetrates the snow surface and the depth at which the station is anchored. Because each successful GNSS reflection yields an individual h_R estimate, which is collected at different azimuths around the station, a map of the receiver station's surrounding topography can be made. This would provide a much greater spatial resolution of snow and sea ice conditions than that of remote sensing observations. However, the SIDEx network only spans ~5 km, and the receiver stations are not uniformly distributed in this space. Future studies should explore the possibility of creating a practical map of the sea ice surface using individual GNSS reflections by crafting a larger network with more receiver stations.

To fully validate the GNSS-IR h_R measurements, in-situ measurements are required at each of the SIDEx stations. Although the IMB data provides snow depth measurements, they are taken over 10 km away from the SIDEx receivers that are used for GNSS-IR, so the accuracy of GNSS-IR snow depth measurements cannot be truly confirmed. Remote sensing observations, including measurements of snow depth and images of the region, should also be incorporated to confirm these possible events, changes in the snow, and potential melt ponding. However, the remote sensing observations may lack the resolution to demonstrate the changes in the snow and/or ice for SX15. Lastly, additional GNSS-IR observations should be obtained to gain more information about winter and summer h_R.

CONCLUSION

Since its conception 30 years ago (Martin-Neira 1993), GNSS-IR has developed to provide a myriad of environmental measurements using existing GNSS infrastructure. Although the technique has been previously applied to stationary receiver antennas, calculating h_R for a dynamic station has proved to be effective as well, as explored with the SIDEx. The GNSS-IR technique yielded h_R estimations with centimeter-level precision, which were then improved with a model detrending using azimuth. Furthermore, spatiotemporal differences and snow events were observed using the technique, corresponding to in-situ measurements recorded during the experiment. This study has demonstrated the capabilities of applying GNSS-IR for monitoring snow, beyond traditional scenarios. It opens the door to precise and frequent measurements in extremely remote locations, at an affordable cost. As the consequences of climate change continue to worsen, it is important to closely monitor snow events, especially in the Arctic with the effects of Arctic amplification, so GNSS-IR is a promising outlet for future data collection and research.

ACKNOWLEDGEMENTS

This work is supported under the Office of Naval Research (ONR) award (N000141912605) "The Integrated Sea Ice Dynamic Experiment (SIDEx)” and under a National Science Foundation (NSF) Research Experience for Undergraduates (REU), both to MIT Haystack Observatory. Thank you to Dhiman Mondal, Pedro Elosegui, Chet Ruszczyk, and John Barrett at MIT Haystack Observatory for teaching me all about GNSS-IR and mentoring me in this project. I would also like to thank Manuela Girotto and the Girotto Lab for their support, feedback throughout my project, and the initial opportunity to get started in cryospheric research. Additionally, thank you to the ESPM 175 teaching team, especially Danielle Perryman and Tina Mendez, for their encouragement, feedback, and enthusiasm this past year. Last, but not least, thank you to my friends and family who have supported and believed in me throughout my time at UC Berkeley. Even though a sizable portion of it was remote, I still have so many fond memories from my time here, and I could not have made it this far without you all!

REFERENCES

Dahl-Jensen, T. S., M. Citterio, J. Jakobsen, A. P. Ahlstrøm, K. M. Larson, and S. A. Khan. 2022. Snow Depth Measurements by GNSS-IR at an Automatic Weather Station, NUK-K. Remote Sensing 14:2563.

Gutmann, E. D., K. M. Larson, M. W. Williams, F. G. Nievinski, and V. Zavorotny. 2011. Snow measurement by GPS interferometric reflectometry: an evaluation at Niwot Ridge, Colorado. Hydrological Processes 26:2951–2961.

Hwang, B., J. Wilkinson, T. Maksym, H. C. Graber, A. Schweiger, C. Horvat, D. K. Perovich, A. E. Arntsen, T. P. Stanton, J. Ren, and P. Wadhams. 2017. Winter-to-summer transition of Arctic sea ice breakup and floe size distribution in the Beaufort Sea. Elementa: Science of the Anthropocene 5:40.

Kacimi, S., and R. Kwok. 2022. Arctic Snow Depth, Ice Thickness, and Volume From ICESat-2 and CryoSat-2: 2018–2021. Geophysical Research Letters 49.

Kohler, J., O. Brandt, M. Johansson, and T. Callaghan. 2006. A long-term Arctic snow depth record from Abisko, northern Sweden, 1913–2004. Polar Research 25:91–113.

Kumar, A., J. Perlwitz, J. Eischeid, X. Quan, T. Xu, T. Zhang, M. Hoerling, B. Jha, and W. Wang. 2010. Contribution of sea ice loss to Arctic amplification. Geophysical Research Letters 37.

Larson, K. M. 2016. GPS interferometric reflectometry: applications to surface soil moisture, snow depth, and vegetation water content in the western United States. WIREs Water 3:775–787.

Larson, K. M. 2022, August 8. kristinemlarson/gnssrefl. Python.

Larson, K. M., and F. G. Nievinski. 2013. GPS snow sensing: results from the EarthScope Plate Boundary Observatory. GPS Solutions 17:41–52.

Ledley, T. S. 1991. Snow on sea ice: Competing effects in shaping climate. Journal of Geophysical Research: Atmospheres 96:17195–17208.

Martin-Neira, M. 1993. A Passive Reflectometry and Interferometry System (PARIS): Application to Ocean Altimetry. ESA Journal 17.

NASA Crustal Dynamics Data Information System. 2020. Global Navigation Satellite System (GNSS) Overview. https://cddis.nasa.gov/Techniques/GNSS/GNSS_Overview.html.

Nievinski, F. G., and K. M. Larson. 2014. Forward modeling of GPS multipath for near-surface reflectometry and positioning applications. GPS Solutions 18:309–322.

Oxley, A. 2017. L1 Frequency - an overview | ScienceDirect Topics. https://www.sciencedirect.com/topics/mathematics/l1-frequency.

Perovich, D. K., T. C. Grenfell, B. Light, B. C. Elder, J. Harbeck, C. Polashenski, W. B. Tucker III, and C. Stelmach. 2009. Transpolar observations of the morphological properties of Arctic sea ice. Journal of Geophysical Research: Oceans 114.

Perovich, D. K., T. C. Grenfell, J. A. Richter-Menge, B. Light, W. B. Tucker III, and H. Eicken. 2003. Thin and thinner: Sea ice mass balance measurements during SHEBA. Journal of Geophysical Research: Oceans 108.

Perovich, D., C. Polashenski, A. Arntsen, and C. Stwertka. 2017. Anatomy of a late spring snowfall on sea ice. Geophysical Research Letters 44:2802–2809.

Previdi, M., K. L. Smith, and L. M. Polvani. 2021. Arctic amplification of climate change: a review of underlying mechanisms. Environmental Research Letters 16:093003.

Purnell, D., N. Gomez, N. H. Chan, J. Strandberg, D. M. Holland, and T. Hobiger. 2020. Quantifying the Uncertainty in Ground-Based GNSS-Reflectometry Sea Level Measurements. IEEE Journal of Selected Topics in Applied Earth Observations and Remote Sensing 13:4419–4428.

Richter-Menge, J. A., D. K. Perovich, B. C. Elder, K. Claffey, I. Rigor, and M. Ortmeyer. 2006. Ice mass-balance buoys: a tool for measuring and attributing changes in the thickness of the Arctic sea-ice cover. Annals of Glaciology 44:205–210.

Roesler, C., and K. M. Larson. 2018. Software tools for GNSS interferometric reflectometry (GNSS-IR). GPS Solutions 22:80.

Southwell, B. J., J. W. Cheong, and A. G. Dempster. 2020. A Matched Filter for Spaceborne GNSS-R Based Sea-Target Detection. IEEE Transactions on Geoscience and Remote Sensing 58:5922–5931.

Sturm, M., and J. Holmgren. 2018. An Automatic Snow Depth Probe for Field Validation Campaigns. Water Resources Research 54:9695–9701.

Tedesco, M., C. Derksen, J. S. Deems, and J. L. Foster. 2015. Remote sensing of snow depth and snow water equivalent. Pages 73–98 Remote Sensing of the Cryosphere. John Wiley & Sons, Ltd.

APPENDIX A: General Sinusoidal Function

$$y = Asin(B(x + C)) + D$$

- A = amplitude
- B = 2π * frequency
- C = phase shift
- D = vertical shift

APPENDIX B: All SIDEx March 2021 h_R Time Series

1.

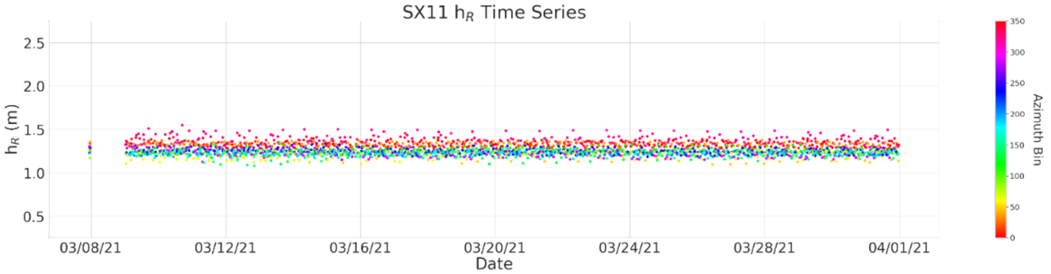

2.

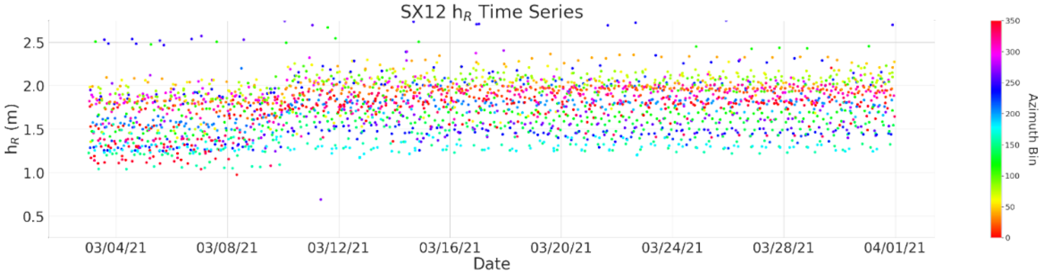

3.

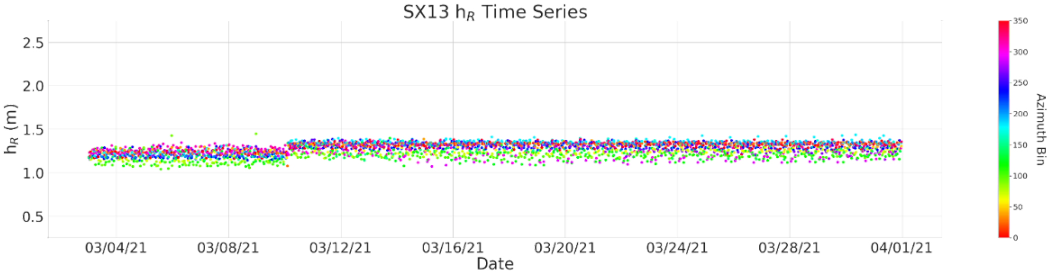

4.

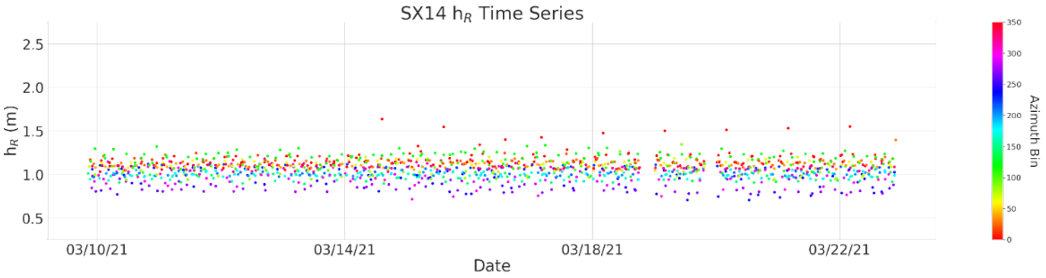
SX14 h_R Time Series
h_R (m)
2.5
2.0
1.5
1.0
0.5
03/10/21
03/14/21
03/18/21
03/22/21
Date
Azimuth Bin
350
300
250
200
150
100
50
0

5.

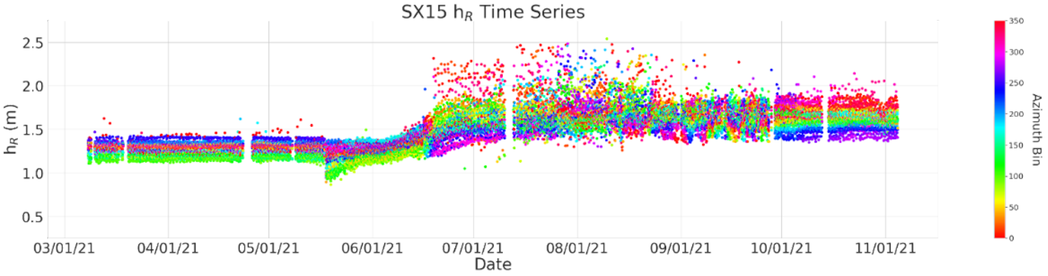
SX15 h_R Time Series
h_R (m)
2.5
2.0
1.5
1.0
0.5
03/01/21
04/01/21
05/01/21
06/01/21
07/01/21
08/01/21
09/01/21
10/01/21
11/01/21
Date
Azimuth Bin
350
300
250
200
150
100
50
0

6.

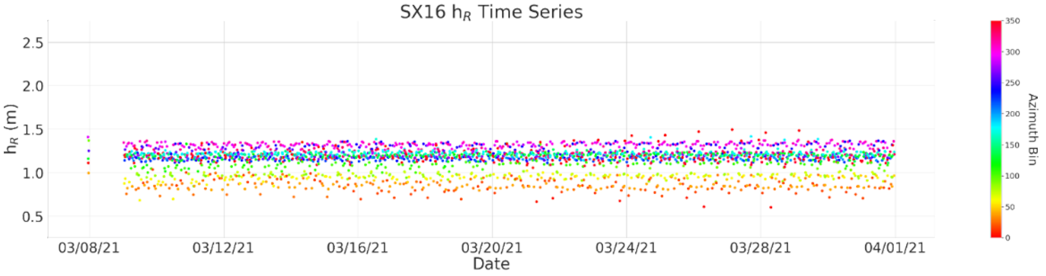
SX16 h_R Time Series
h_R (m)
2.5
2.0
1.5
1.0
0.5
03/08/21
03/12/21
03/16/21
03/20/21
03/24/21
03/28/21
04/01/21
Date
Azimuth Bin
350
300
250
200
150
100
50
0

7.

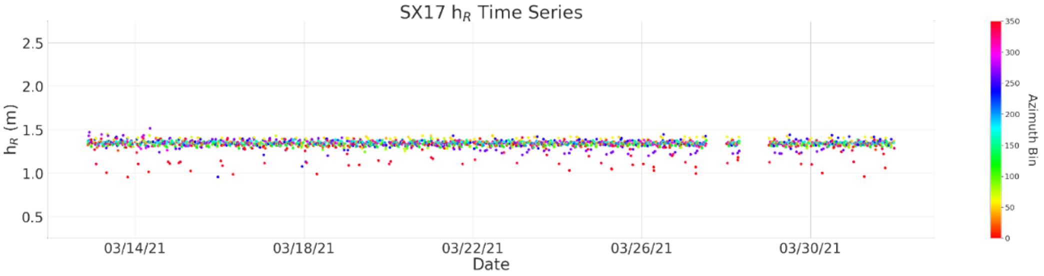
SX17 h_R Time Series
h_R (m)
2.5
2.0
1.5
1.0
0.5
03/14/21
03/18/21
03/22/21
03/26/21
03/30/21
Date
Azimuth Bin
350
300
250
200
150
100
50
0

8.

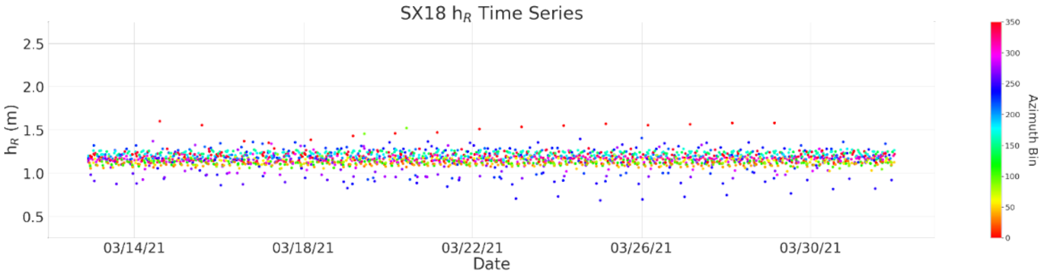
SX18 h_R Time Series
h_R (m)
2.5
2.0
1.5
1.0
0.5
03/14/21
03/18/21
03/22/21
03/26/21
03/30/21
Date
Azimuth Bin
350
300
250
200
150
100
50
0

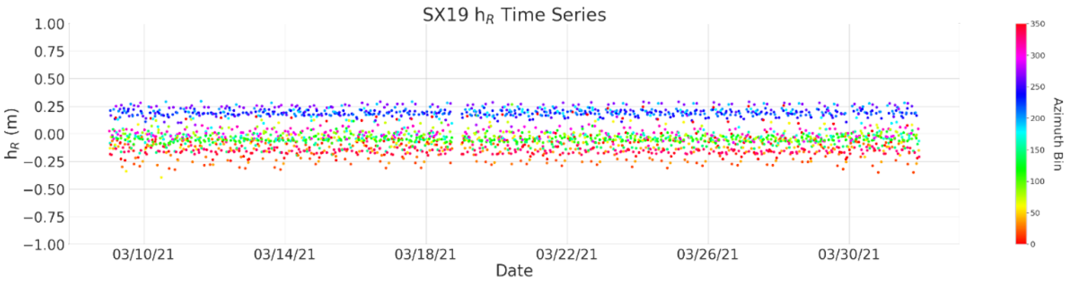

9.

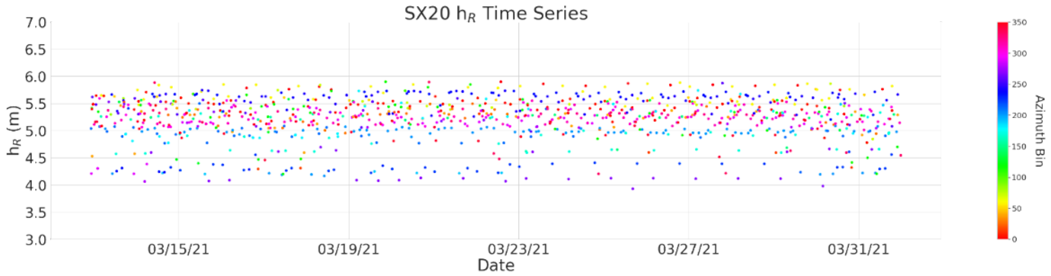

10.

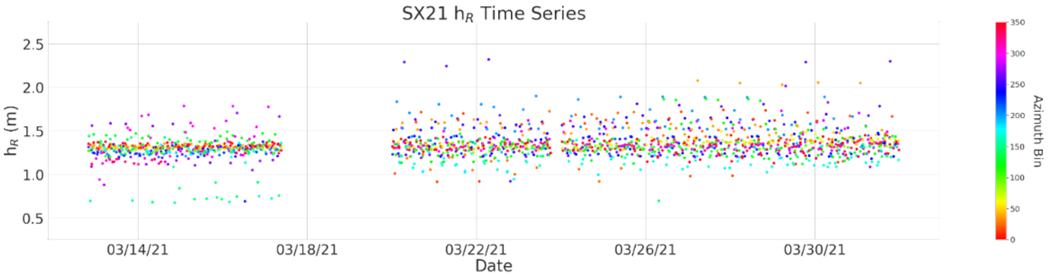

11.

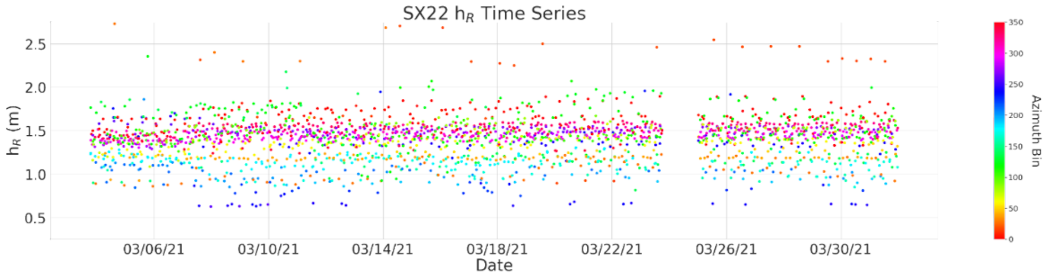

12.

Figure B1-B12. All SIDEx h_R time series. h_R measurements from March 2021, except for SX15, which consists of March to November 2021.

APPENDIX C: All SIDEx March 2021 Average Binned h_R vs Azimuth

1. 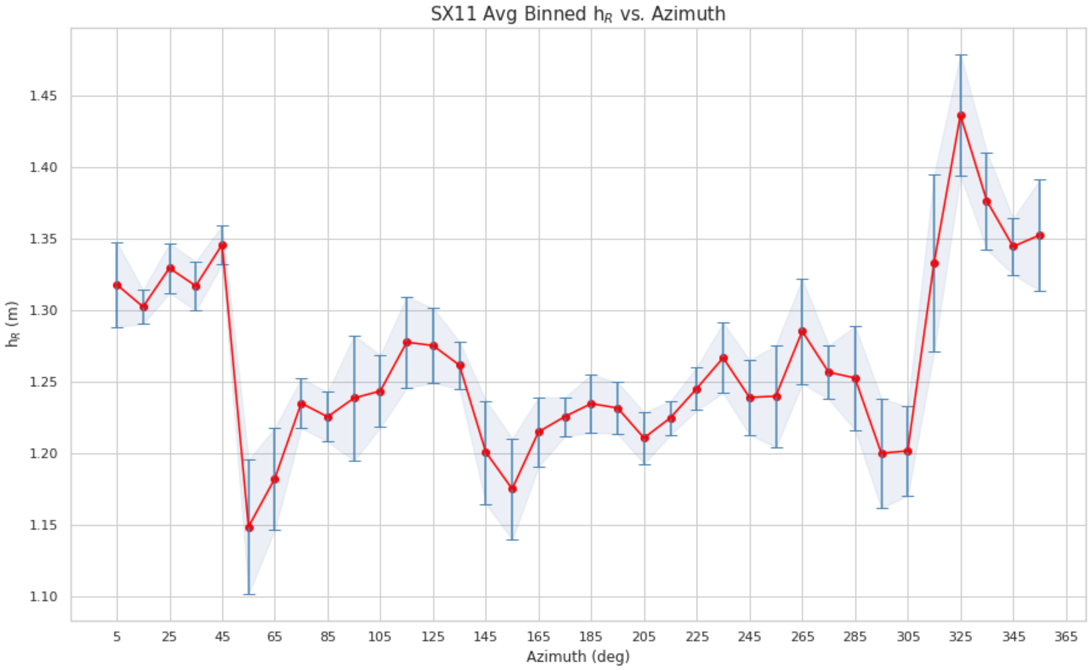

2. 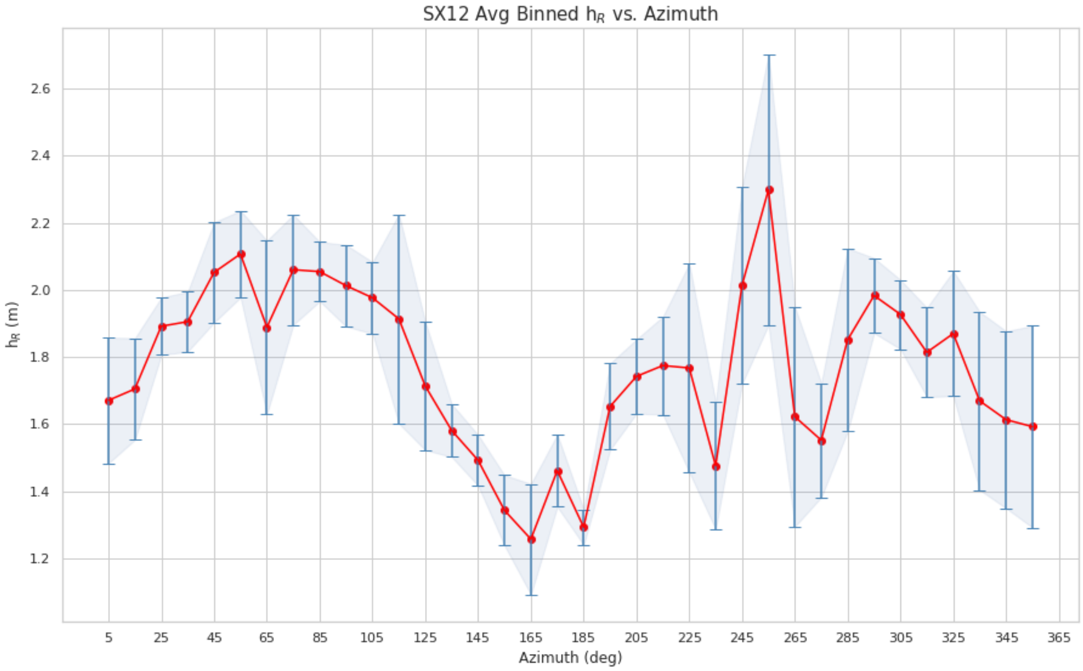

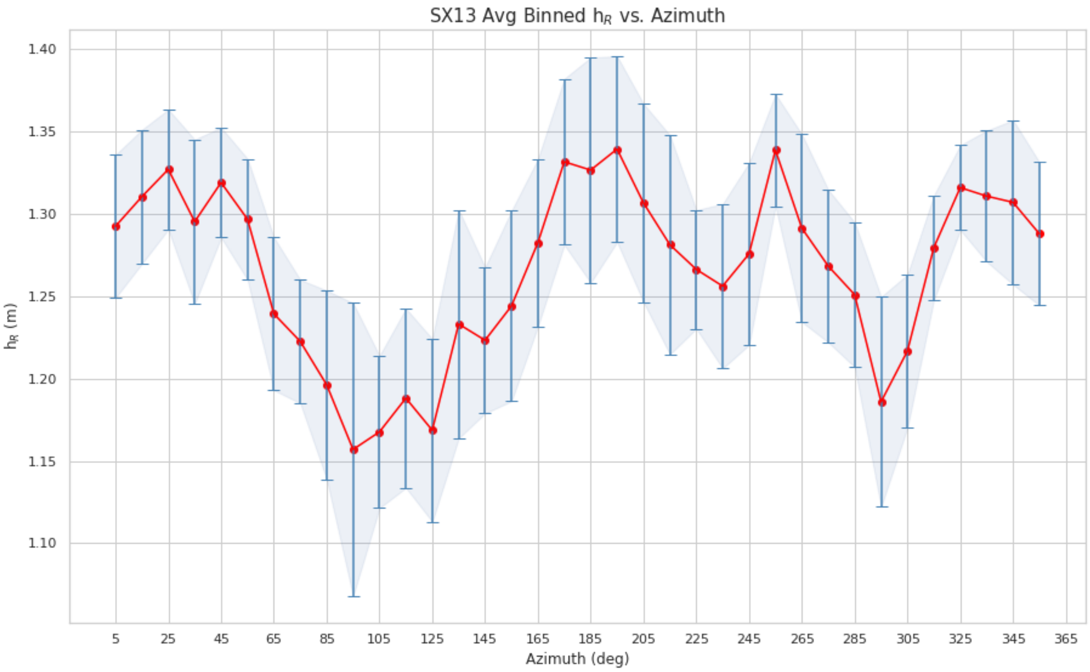
SX13 Avg Binned h_R vs. Azimuth
h_R (m)
1.40
1.35
1.30
1.25
1.20
1.15
1.10
5
25
45
65
85
105
125
145
165
185
205
225
245
265
285
305
325
345
365
Azimuth (deg)

3.

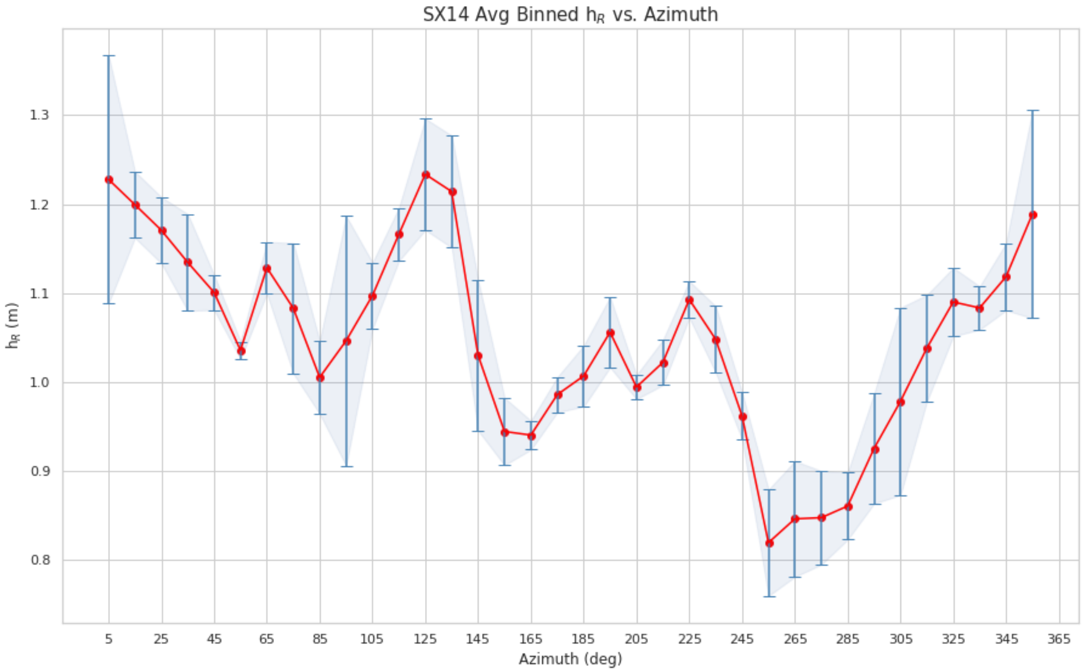
SX14 Avg Binned h_R vs. Azimuth
h_R (m)
1.3
1.2
1.1
1.0
0.9
0.8
5
25
45
65
85
105
125
145
165
185
205
225
245
265
285
305
325
345
365
Azimuth (deg)

4.

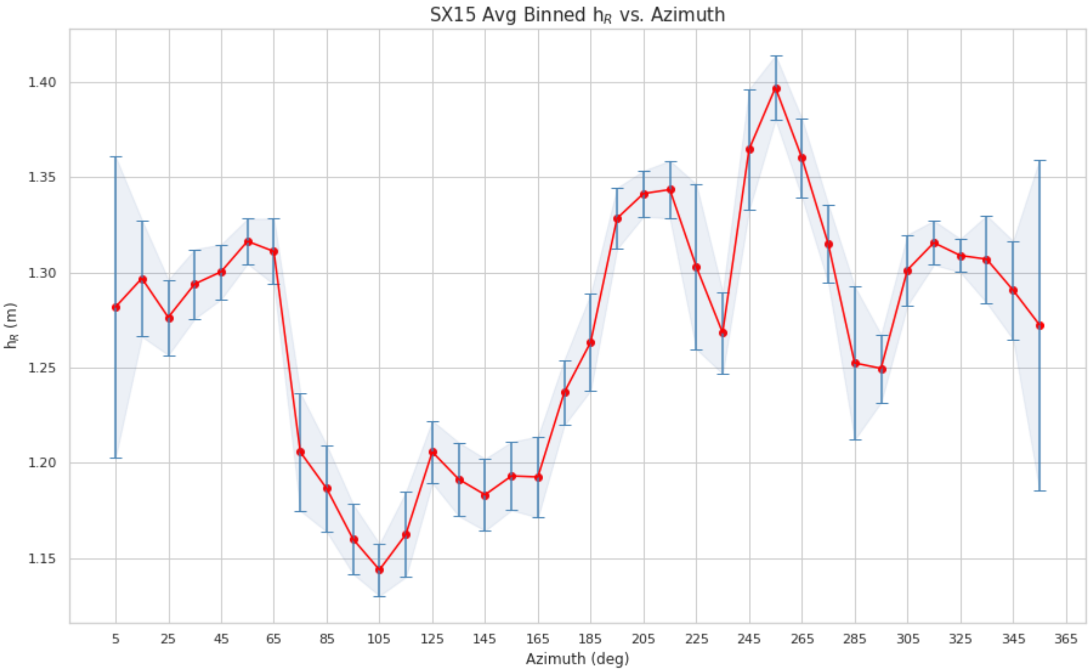
SX15 Avg Binned h_R vs. Azimuth
h_R (m)
1.40
1.35
1.30
1.25
1.20
1.15
5
25
45
65
85
105
125
145
165
185
205
225
245
265
285
305
325
345
365
Azimuth (deg)

5.

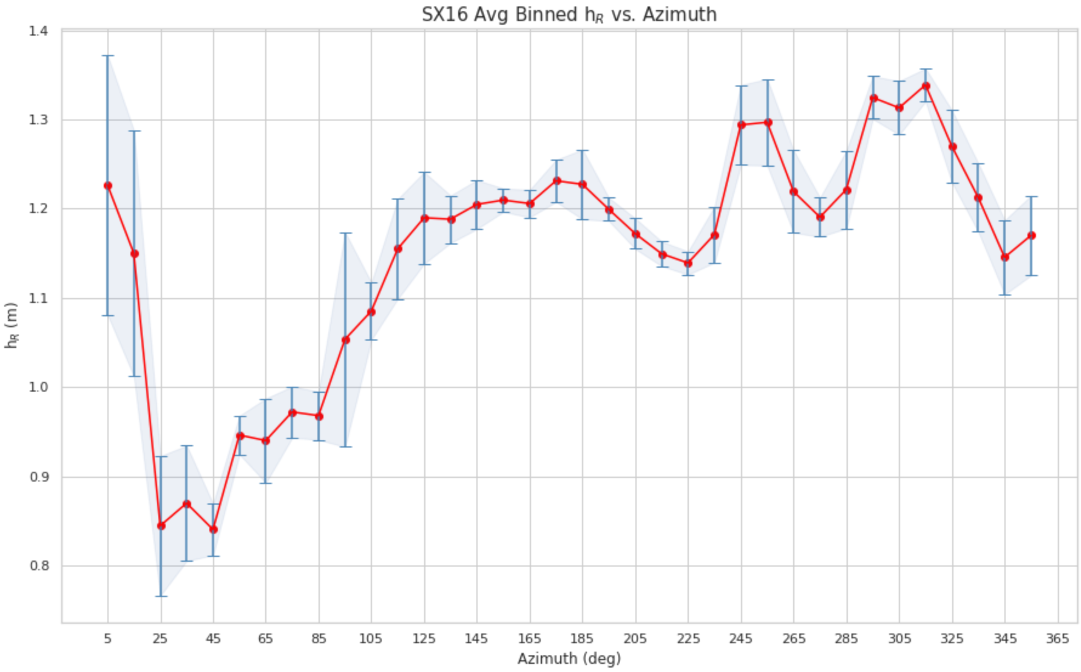
SX16 Avg Binned h_R vs. Azimuth
h_R (m)
1.4
1.3
1.2
1.1
1.0
0.9
0.8
5
25
45
65
85
105
125
145
165
185
205
225
245
265
285
305
325
345
365
Azimuth (deg)

6.

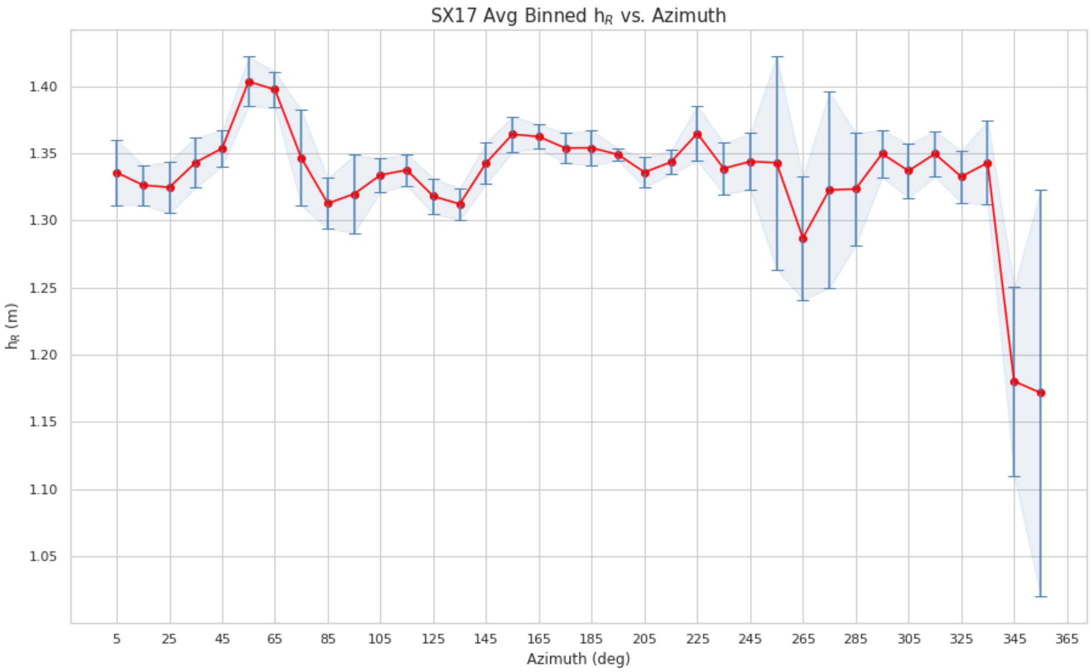
SX17 Avg Binned h_R vs. Azimuth
h_R (m)
1.40
1.35
1.30
1.25
1.20
1.15
1.10
1.05
5
25
45
65
85
105
125
145
165
185
205
225
245
265
285
305
325
345
365
Azimuth (deg)

7.

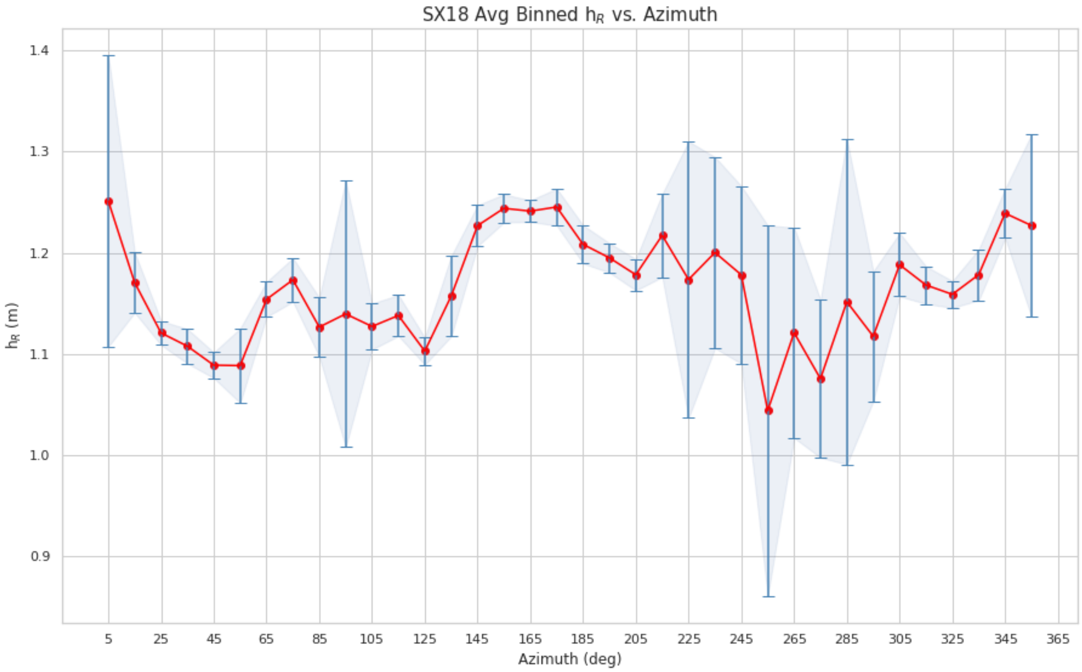
SX18 Avg Binned h_R vs. Azimuth
h_R (m)
1.4
1.3
1.2
1.1
1.0
0.9
5
25
45
65
85
105
125
145
165
185
205
225
245
265
285
305
325
345
365
Azimuth (deg)

8.

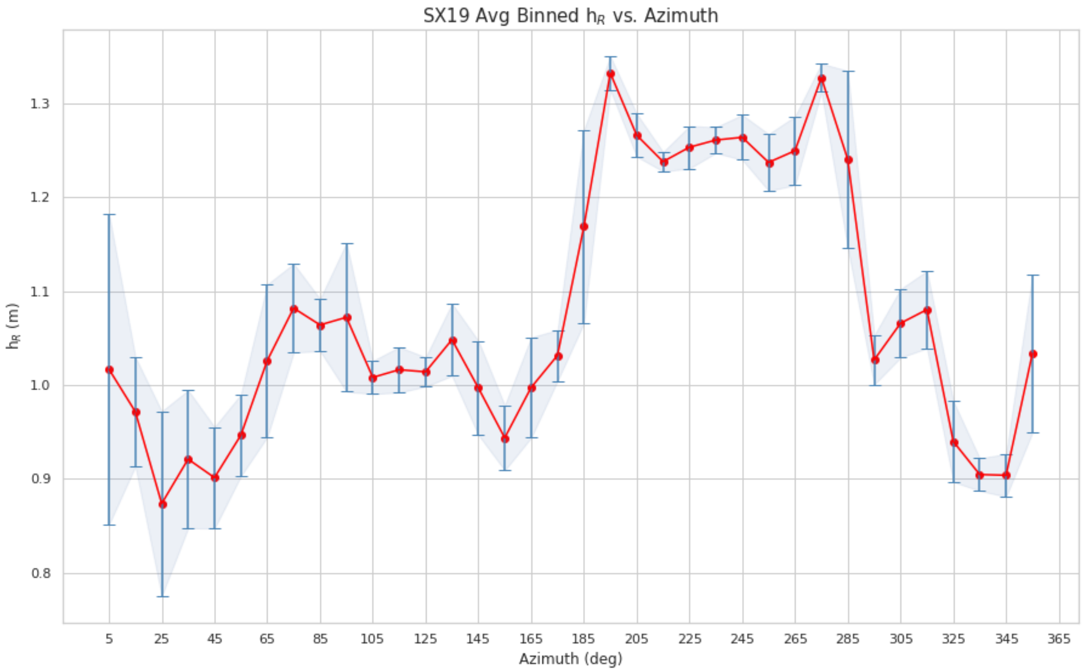
SX19 Avg Binned h_R vs. Azimuth
h_R (m)
1.3
1.2
1.1
1.0
0.9
0.8
5
25
45
65
85
105
125
145
165
185
205
225
245
265
285
305
325
345
365
Azimuth (deg)

9.

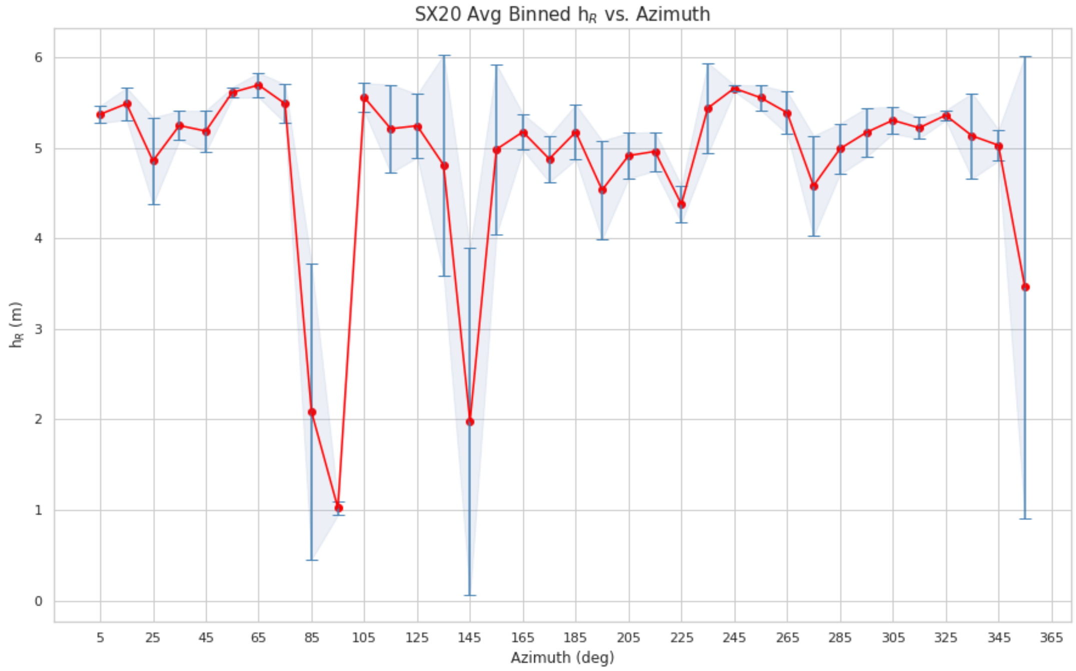
SX20 Avg Binned h_R vs. Azimuth
h_R (m)
6
5
4
3
2
1
0
5
25
45
65
85
105
125
145
165
185
205
225
245
265
285
305
325
345
365
Azimuth (deg)

10.

11.

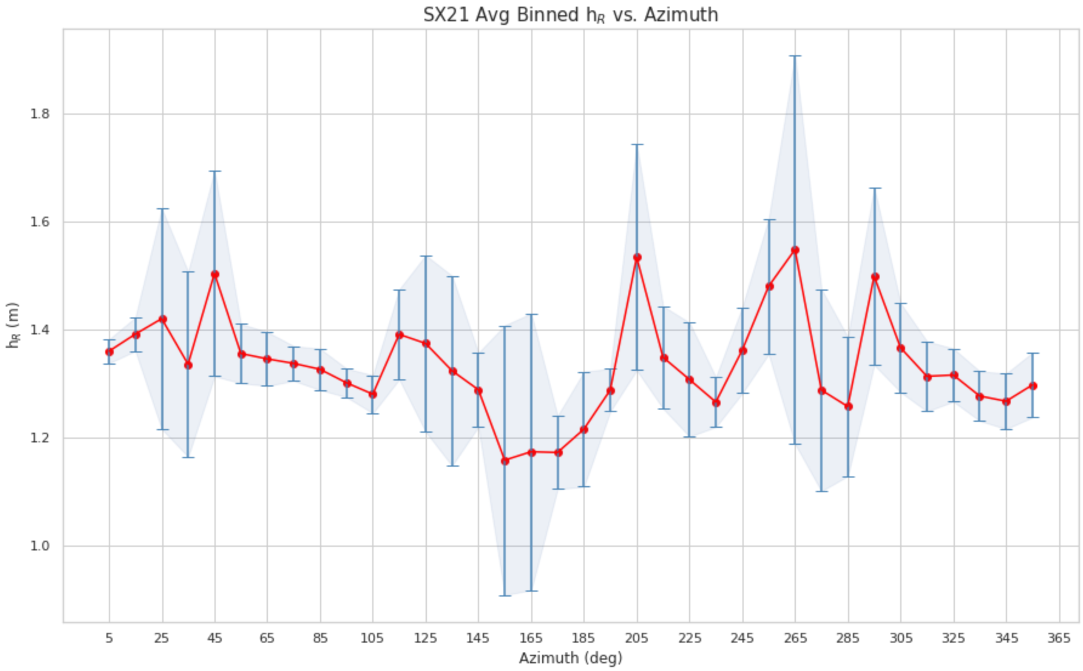

12.

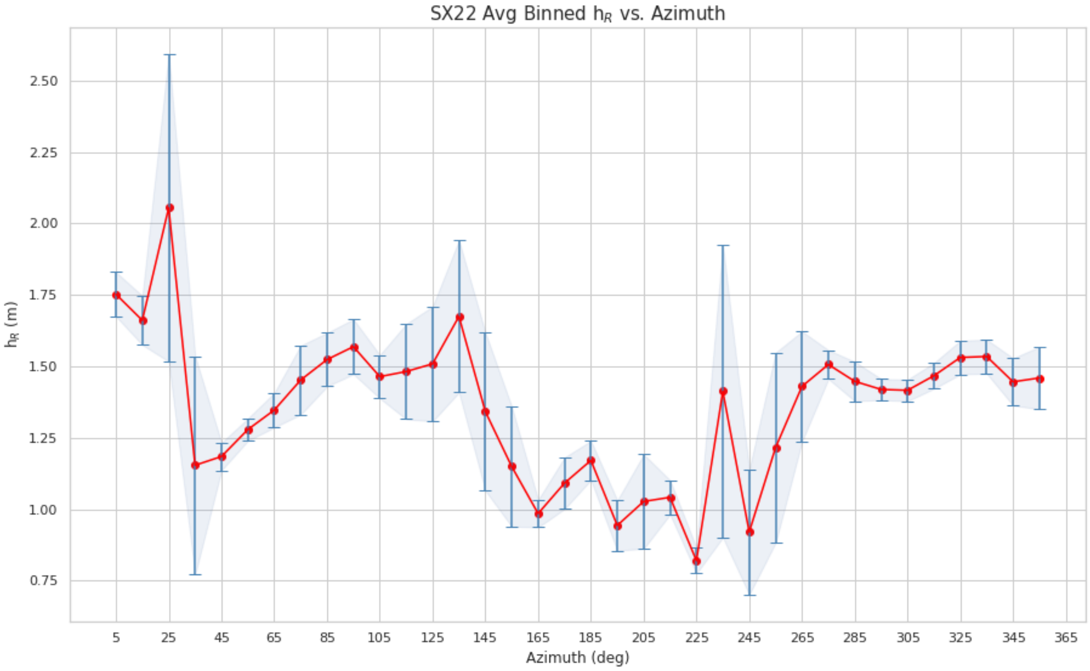

Figure C1-C12. All SIDEx mean h_R by azimuth bins. The mean h_R value is calculated by binning the h_R measurements according to the azimuth at which they were obtained and taking the bin's mean. The standard deviation of each bin is represented by the blue error bars.

APPENDIX D: All SIDEx March 2021 Detrended h_R Time Series

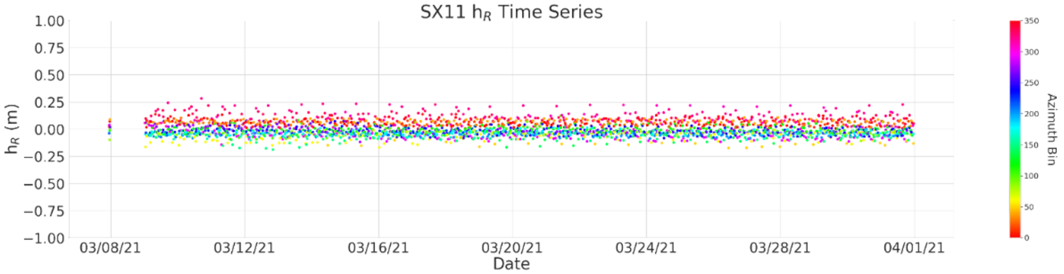

1.

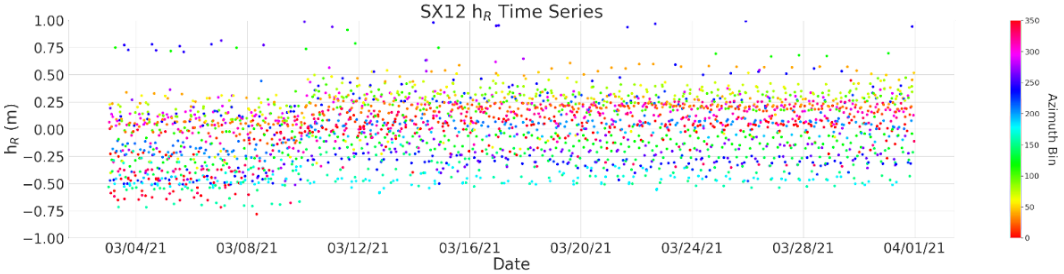

2.

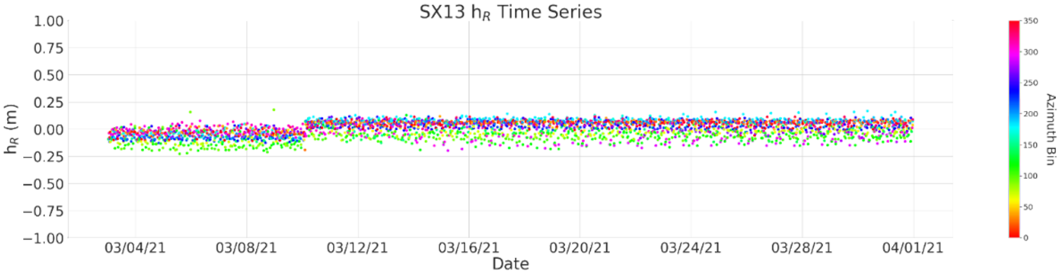

3.

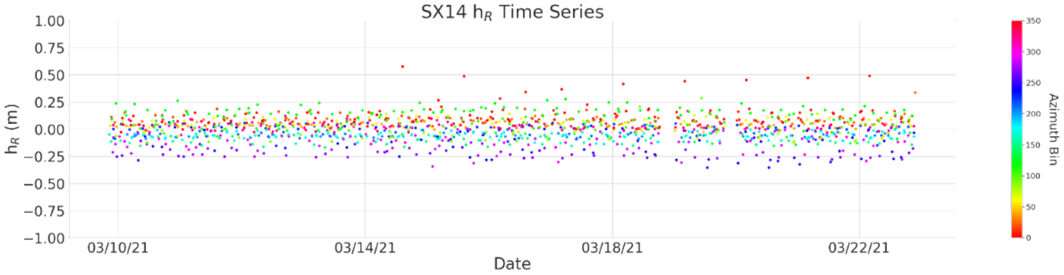

4.

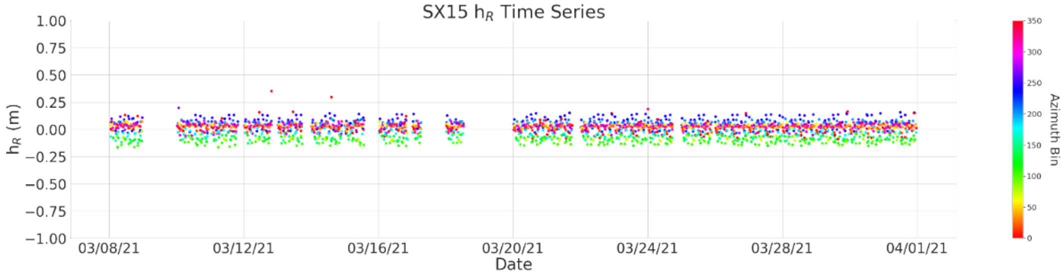

5.

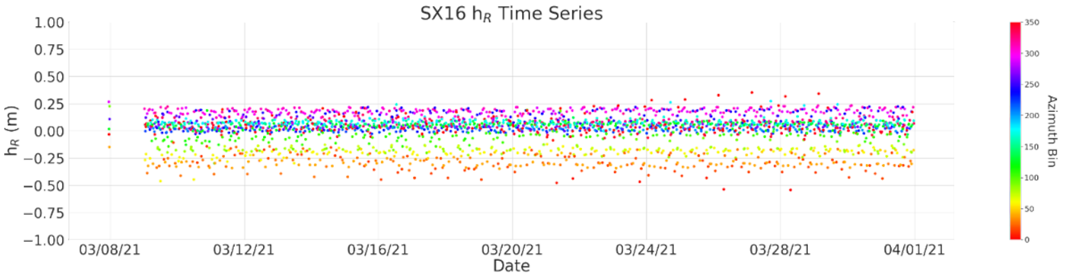
SX16 h_R Time Series
h_R (m)
1.00
0.75
0.50
0.25
0.00
−0.25
−0.50
−0.75
−1.00
03/08/21
03/12/21
03/16/21
03/20/21
03/24/21
03/28/21
04/01/21
Date
Azimuth Bin
0
50
100
150
200
250
300
350

6.

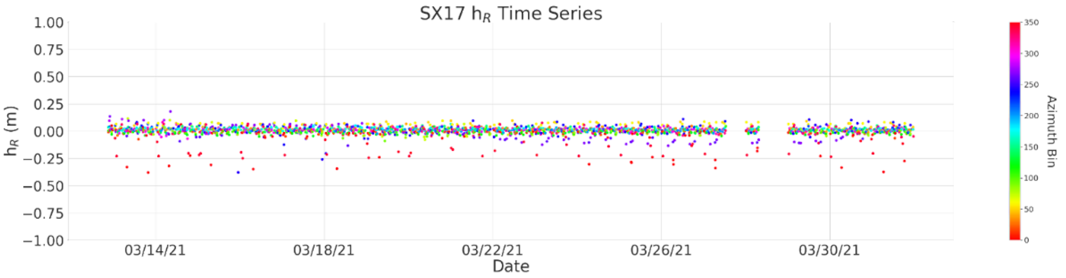
SX17 h_R Time Series
h_R (m)
1.00
0.75
0.50
0.25
0.00
−0.25
−0.50
−0.75
−1.00
03/14/21
03/18/21
03/22/21
03/26/21
03/30/21
Date
Azimuth Bin
0
50
100
150
200
250
300
350

7.

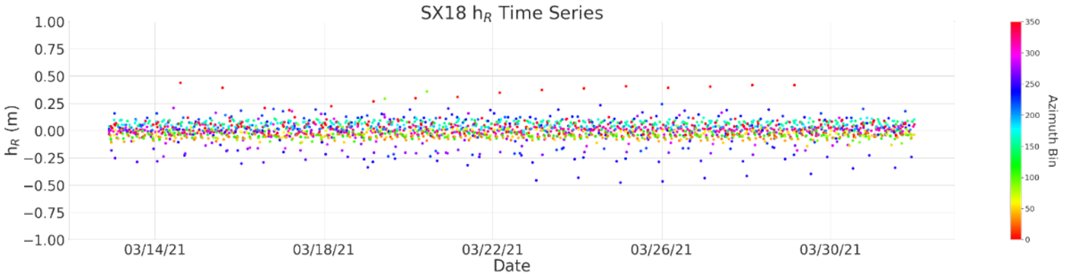
SX18 h_R Time Series
h_R (m)
1.00
0.75
0.50
0.25
0.00
−0.25
−0.50
−0.75
−1.00
03/14/21
03/18/21
03/22/21
03/26/21
03/30/21
Date
Azimuth Bin
0
50
100
150
200
250
300
350

8.

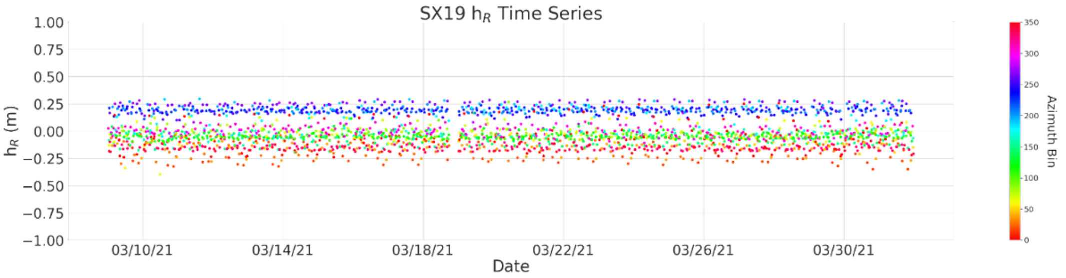
SX19 h_R Time Series
h_R (m)
1.00
0.75
0.50
0.25
0.00
−0.25
−0.50
−0.75
−1.00
03/10/21
03/14/21
03/18/21
03/22/21
03/26/21
03/30/21
Date
Azimuth Bin
0
50
100
150
200
250
300
350

9.

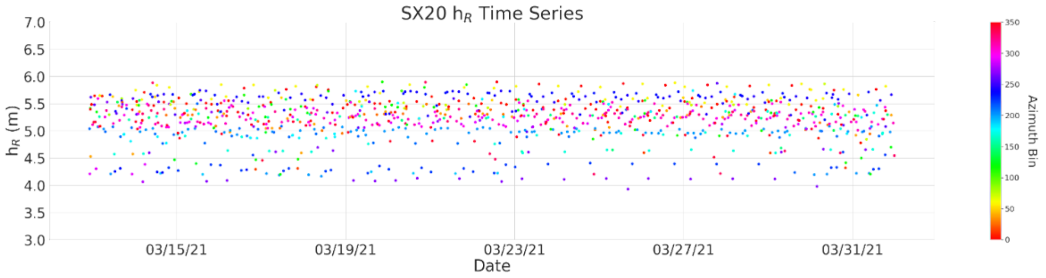
SX20 h_R Time Series
h_R (m)
7.0
6.5
6.0
5.5
5.0
4.5
4.0
3.5
3.0
03/15/21
03/19/21
03/23/21
03/27/21
03/31/21
Date
Azimuth Bin
0
50
100
150
200
250
300
350

10.

11.

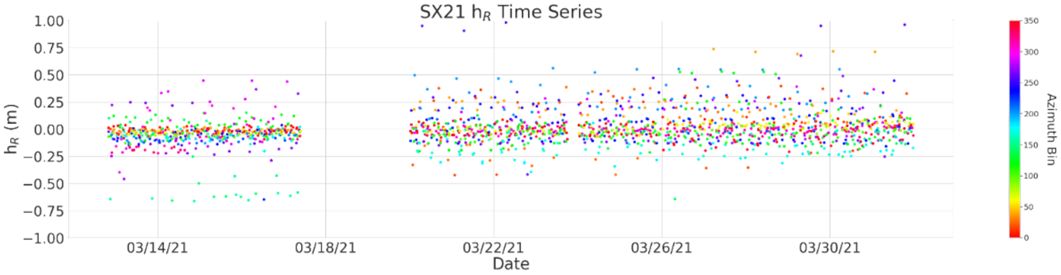

12.

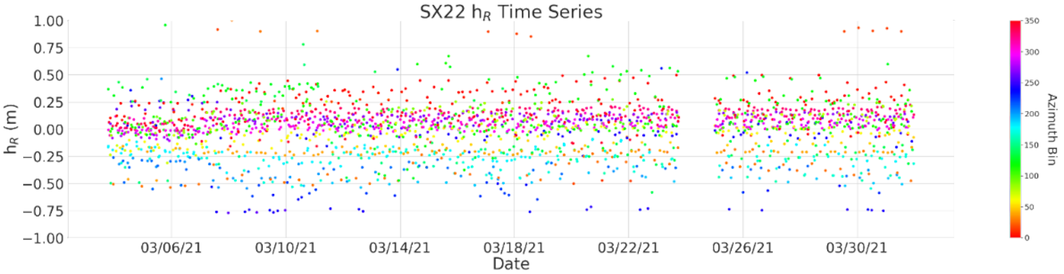

Figure D1-D12. All SIDEx detrended h_R time series. Time series of the detrended h_R measurements from March 2021.